DEVELOPMENT TOWARDS IMPROVED DURABILITY OF IMPLANTED NEUROPROSTHETIC ELECTRODES THROUGH SURFACE MODIFICATIONS

by

Christian Phillip Vetter

A Thesis

Submitted to the Faculty of Purdue University

In Partial Fulfillment of the Requirements for the Degree of

Master of Science in Biomedical Engineering

Department of Biomedical Engineering

Indianapolis, Indiana

August 2020

THE PURDUE UNIVERSITY GRADUATE SCHOOL

STATEMENT OF COMMITTEE APPROVAL

Dr. Ken Yoshida, Chair

Department of Biomedical Engineering

Dr. Babak Anasori

Department of Mechanical and Energy Engineering

Dr. Ed Berbari

Department of Biomedical Engineering

Approved by:

Dr. Julie Ji

Head of the Graduate Program

”I will say of the Lord, He is my refuge and my fortress: my God, in him will I trust.”

- Psalm 91:2, KJV

I dedicate this thesis to those whom have given me strength in times of hardship. My grandparents, for chaperoning my development and my parents for supporting me through all my trials and tribulations. I would especially like to thank my mother, who taught me perseverance and to find the good in all situations. And above all, my Lord and Savior, Jesus Christ, for exchanging his life for my salvation.

ACKNOWLEDGMENTS

I would like to extend my appreciation to Dr. Ken Yoshida for giving me an opportunity to work in the Bioelectronics Laboratory. He has continued to challenge me while providing the necessary scaffolding to grow as a student, intellectual, and mentor. With his guidance, I have grown to understand what seems to be a small, yet vital, fraction of the complex field of bioelectronics and its application to the study of neuromodulation of the peripheral nervous system. Albeit complex and ever-expanding, I have come to realize how to make sense of what was once mysterious and completely unknown.

I would like to thank my colleagues and friends in the Bioelectronics Laboratory: Awadh Al-Hawwash, Ivette Muzquiz, Lindsey Richardson, Ryne Horn, Onna Doering, Macallister Smolik, Christopher Hoffman, Tyler Fears, Tyler Johnson, Nathaniel Lazorchak, and Justin Parks. A very special thank you to Dr. Carol Bain from the Histotechnology program at the Indiana University School of Medicine for her guidance in the development of the histology protocols in our lab for use in analyzing peripheral nerve physiology. An extended thanks to Tyler Fears, Tyler Johnson, and Justin Parks for assisting with the progression of this protocol.

This work was supported by the Defense Advanced Research Projects Agency, LUNA Innovations, and the National Institute for Health.

TABLE OF CONTENTS

LIST OF TABLES

LIST OF FIGURES

LIST OF ABBREVIATIONS

AC	Alternating Current
Ag/AgCl	Silver/Silver-Chloride
Au	Gold
CB	Carbon Black
cNT	Carbon Nanotubes
DARPA	Defense Advanced Research Project Agency
DC	Direct Current
EDOT	Ethylenedioxythiophene
ICP	Intrinisically Conductive Polymer
IUPAC	International Union of Pure and Applied Chemistry
LFAC	Low-Frequency Alternating Current
PEDOT	Poly(Ethylenedioxythiophene)
PNS	Peripheral Nervous System
PPy	Polypyrrole
PSS	Polystyrene Sulfonate
Pt	Platinum
SS	Stainless-Steel
US	United States

ABSTRACT

Vetter, Christian Phillip M.S.B.M.E., Purdue University, August 2020. Development Towards Improved Durability of Neuroprosthetic Electrodes Through Surface Modification. Major Professor: Dr. Ken Yoshida.

The present thesis was completed to satisfy two functions in our laboratory: (1) explore carbon-black (CB) as an additive for electrodeposited intrinsically conductive polymers (ICPs) to improve electrical properties across the electrode-electrolyte interface for use in neuromodulation; and (2) design a histology protocol that will analyze peripheral nerve system (PNS) tissue following implantation of conventional metal and modified conventional metal electrodes with the ICP poly(3,4-ethylenedioxythiophere):poly(styrenesulfonate)/carbon-black (PEDOT:PSS/CB). It would appear that the functions explored may seem unrelated, however, these two topics play a crucial role in designing a viable electrode for use in acute and chronic neuromodulation and the subsequent analysis required to determine the mechanical properties and overall biocompatibility of design.

A series of experiments with different PEDOT:PSS solutions containing varying amounts of suspended CB (n=19; 0 mg/mL to 2 mg/mL) were explored. Solutions were characterized using cyclic voltammetry (CV) using the intended electrode for deposition, composed of stainless-steel (SS), as the working electrode (WE) to determine respective redox potentials. SS was chosen because of its inherently bad electrochemical properties, meaning that improved functionality post electrodeposition would be easy to identify. Immediately following CV, stainless-steel electrodes were electrodeposited using one of two techniques: (1) potentiostat, allowing the cell to rest at the redox potential required for bipolaron formation (0.9 V); or (2) galvanostat, where the electrode was submitted to a constant current of 200 μA and allowed to coat. Rapid electrochemical impedance spectroscopy was performed prior to and immediately following coating to determine the pre-electrochemical and post-electrochemical impedance characteristics. Results indicate that there was a positive relationship between the amount of CB additive and the relative impedance drop between the uncoated and coated counterparts. Furthermore, the modified electrochemical interfaces are substantially improved for use in frequency ranges of 10 Hz to 50 kHz, which encompass the ranges of our labs recently discovered low frequency alternating current (LFAC) for use in neuromodulation; thus indicating that PEDOT:PSS/CB modification may be used to improve impedance characteristics during our future LFAC experiments. This protocol, the one that contains the ideal concentration of carbon-black, was then recorded and will be used in our lab.

Histology protocols were developed to improve our labs capabilities of post-mortem analysis of PNS tissue. Processing and embedding preparations that explored included paraffin, acrylic, and frozen. Subsequently, staining protocols were developed; however, they varied as a function of the embedding media used; staining protocols developed incorporated progressive and regressive hematoxylin and eosin (H&E) staining as well as toluidine blue (TB). Tissue was sectioned and observed using light microscopy.

CHAPTER 1. INTRODUCTION

Neuromodulation is defined as using an externally generated electrical signal to target, stimulate, and thereby alter the function of the nervous system; stimulation can be achieved through invasive or non-invasive means. The injection of current from an external power supply that subsequently elicits a controlled, tuneable response in the nervous system is the hallmark of biological implantable electrical systems. The process through which this occurs is relatively straight forward; externally generated current alters the contemporaneous activity of the nervous system, which is outlined by a conduction pathway analagous to how electricity moves through a wire. However, the mechanisms through which this occurs is much more complex and relies on conduction of ions rather than conduction of electrons.

One of the most difficult problems explored by biomedical experts in the field of neural engineering is how to develop an inexpensive and efficient technology that bridges the gap between the implantable system (man-made) and the biological target. The scope of this problem is extremely broad and bridges many areas of research such as cellular pathophysiology, histotechnology, neuroscience, neural engineering, and biomedical design. In the present, we are exploring flexible methods to explain the effects of geometry of the neurointerface. Once identified, a better manufacturing method can be used for long term analysis.

The following dissertation provides a brief review of implantable systems and their electrochemical interfaces, outlining work performed in the Bioelectronics Laboratory at Indiana University Purdue University, Indianapolis to improve the durability and charge transfer characteristics of conventional electrodes used in neuromodulation through addition of an additive, carbon black, to a synthetic conductive polymer mixture, Poly(3,4-ethylenedioxythiophere):poly(styrenesulfonate) (PEDOT:PSS). Secondly, to evaluate the host-response of the modified electrodes, a histology technique was developed to study tissue characteristics at the electrode-nerve interface.

1.1 Advent of Implantable Neuromodulatory Systems

Since the onset of the field in the early 1960's, neuromodulation has been used to study neural anatomy and treat various disease pathologies. Most recently, applications have grown to include neuroprosthetics and the developing technology of implantable brain-machine interfaces. However, before one can understand the methods through which neuromodulation achieves its desired results, it is important to mention its original goal and reason for development: to treat chronic pain [1].

The nervous system is the organ responsible for how nearly all multicellular organism control, communicate, and interact with their environment and, in the case of neurmodulation, can be commandeered to elicit change in the organism. Prior to the development of electrophysiology, the branch of physiology that studies the electrical properties of biological systems, there was a belief that animals were controlled by "animal spirits" responsible for nerve conduction [2]. Electrophysiology, founded by Luigi Galvani in 1771, put an end to the mysterious and popular belief of "animal spirits." This was most notably disputed in what came to be known as Galvani's first experiment when he proved the influence of electricity on a frog crural nerve by stimulating it through means of an externally generated current and recording its subsequent muscle contraction [1, 2].

Nearly a century after Galvani made his initial discovery, scientists began exploiting the electrophysiology of the brain. In 1870, Fritsch and Hitzig stimulated the motor cortex of a dog by contracting one of its limbs [1, 3]. Shortly thereafter, the technique was further carried out by Bartholow (1874) on the brain of an awake human, the first of its kind [1, 4, 5]. A decade later, Sir Victor Horsley stimulated the occipital encephalocele and recorded bilateral fixation of the eyes [1]. In 1886, he became the first individual to use intraoperative stimulation, identifying the thumb cortical area for abscission to treat a patient with epilepsy [1, 6].

In 1908, Sir Victor Horsley and Robert Clark developed stereotactic surgery, a minimally invasive surgical method performed to locate and map targets within in the brain [1, 7]. Despite their discovery, this operation was not performed on humans until 1947 by Spiegel and Wycis [1, 8]. Around the same time, a graduate student by the name of Rudolph Hess recognized that stimulation methods, such as those applied by Spiegel and Wycis, may alter effects depending on stimulation frequency, resulting in either stimulus enhancement or inhibition [1]. These contributions eventually led to the understanding of pain perception. In 1965, the gate-theory of pain was proposed by Ronald Melzack and Patrick Wall. Their theory suggested that pain is an interaction between a gate control system that lies within the substantia gelatinosa which modulates afferent patterns that lead to selective activation of brain processes, further activating neural mechanisms that control the response and perception of pain [9]. The gate is controlled by a balance between the firing of large and small fibers; stimulation of large fibers closes the gate, leading to a more pleasurable response [1].

Gate theory led to the development of transcutaneous stimulation (TENS). TENS was tested in 1967 by Wall and Sweet who recruited Roger Avery to design an implantable simulator to be used to treat chronic pain via peripheral nerve stimulation, giving birth to the field of neuromodulation [1]. Around the same, Norman Shealy at Western Reserve Medical School proposed using TENS to stimulate large nerve fibers in the spinal cord. Shealy elicited the help of Medtronic, whereby they repurposed a device used for cardiovascular indications to attenuate peripheral nerve injury. As a result, Shealy was ultimately credited with the discovery of the modern TENS unit and is further regarded as the founder of implantable neuromodulatory devices as they are known today [1].

1.2 Foundations of Neural Interfaces: Recording and Stimulation

The underlying mechanism of neural modulation is the transfer of charge from the source electrode to the recipient nerve. Prior to reaching the nerve, the current must conduct ionically through an electrolytic solution, and depending on electrode placement, transcutaneously and across the outer and innermost layers of the nerve bundle. Despite the numerous locations electrodes may be placed, the current study focus' on the extrafascicular (outside of the fascicle) and intrafascicular (within the fascicle) nerve domain. These electrode-electrolyte interfaces have been extensively studied, however continue to be challenging to model as it varies on a number of factors, a few of which are outlined in the present [10–13].

A variety of equivalent circuits have been proposed to describe the electrode-electrolyte relationship. In their most basic form, they are composed of a double-layer (non-Faradaic) impedance in parallel to a Faradaic impedance, which are both in series with a solution impedance (1.1a). Solution impedance is a result of the presence or absence of ionic charge carriers in the electrolytic solution. The double-layer impedance is the non-reactive component that results from two parallel layers of charge. The first layer is a polarized layer of solvent ions resulting from attraction to an oppositely charged surface. The second layer results from a wall of charges that oppose the first, sandwiching the solvent layer between an oppositely charged surface referred to as the inner and outer Helmholtz planes, respectively (1.1b). Lastly, Faradaic impedance arises when the charged electrode surface has redox potential. To better define Faradaic impedance, it is what occurs as a result of a reaction at the surface of the electrode. As the electrons are passed into (cathode) or taken up from (anode) the solution, they may obtain an electrochemical potential large enough to breach the activation energy to initiate neighboring components in the electrolyte to react with the surface of the electrode. These three impedance's are the principle variables behind all electrochemical processes, and can be described in a number of different ways.

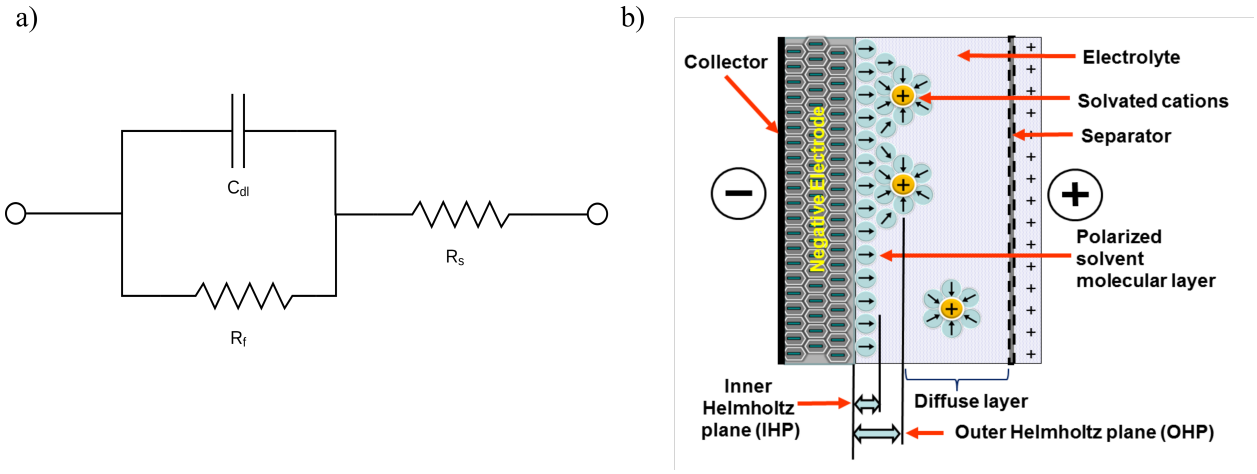

Figure 1.1. (a) The equivalent circuit diagram; composed of a double layer capacitance (C_{dl}) parallel to a Faradaic resistance (R_f), both of which are in series with the resistance of the solution (R_s). (b) Depiction of electrode-electrolyte boundary where a double-layer capacitance forms (C_{dl}); adapted from [14].

Apprehension of the Faradaic mechanisms at the surface of an electrode are essential for understanding the chemical information of the system. By definition, a Faradaic process must result in an electronic charge being injected into or out of the electrode from the bulk solution, and not stored charge as in a non-Faradaic process [15]. This electronic charge transfer involves the atoms and ions or molecules, such as products or reactants of the redox exchange between bulk media and the electrode surface; redox reactions within the electrode or at its surface alone does not imply a Faradaic process, a charge transfer between the bulk media and electrode must occur. On the other hand, a non-Faradaic charge results in a double layer capacitance that was previously described in Fig. 1.1b. The difference between a non-Faradaic and Faradaic system is depicted in Fig. 1.2 [15]. For further information on this subject, texts which outline the mechanism of Fardaic and non-Faradaic charge transfers in detail are Mohilner (1966), Erdey-Grúz (1972), and Bard and Faulkner (1980) [15–18].

In neuromodulation, it is current that delivers the necessary energy to elicit a change in the physiology of the targeted system. Non-Fardaic processes result in storage of ions and a buildup of charge in polarizable solutions, such as those found within the body. In neural interfaces, Non-Faradaic porcesses lead to a double-layer discharge, sustains small alternating currents (AC), and does not allow for direct currents (DC). On the contrary, a Faradaic process will not succumb to a buildup of charge and steady-state current will not result in a compositional change of the electrode. Fig. 1.2 depicts the response to a step change in voltage; in a typical cell, a slight (polarizable) capacitive change occurs until it reaches a new equilibrium, an increased current. The settling of this charge is a function of a time constant associated with a high pass filer, resulting in the delay in the return to equilibrium. To provide the greatest charge transfer across the electrode and bulk media, it would be ideal to use a non-polarizable electrode; however, the most effective non-polarizable electrodes (such as Ag/AgCl or Pt/PtCl) tend to be hazardous to the cell. In the case of a Ag/AgCl electrode, Ag+ is a neurotoxin and Pt/PtCl is susceptible to corrosion. On the contrary, charge buildup in a predominantly non-Faradaic environment leads to complications that may result in potentially hazardous conditions for the biological tissue of interest as well as a decrease in viability of the working electrode. This charge buildup response occurs when the system undergoes a step change, is depicted in the polarizable electrode illustration in Fig. 1.2, and can be calculated as the area under the current-time curve.

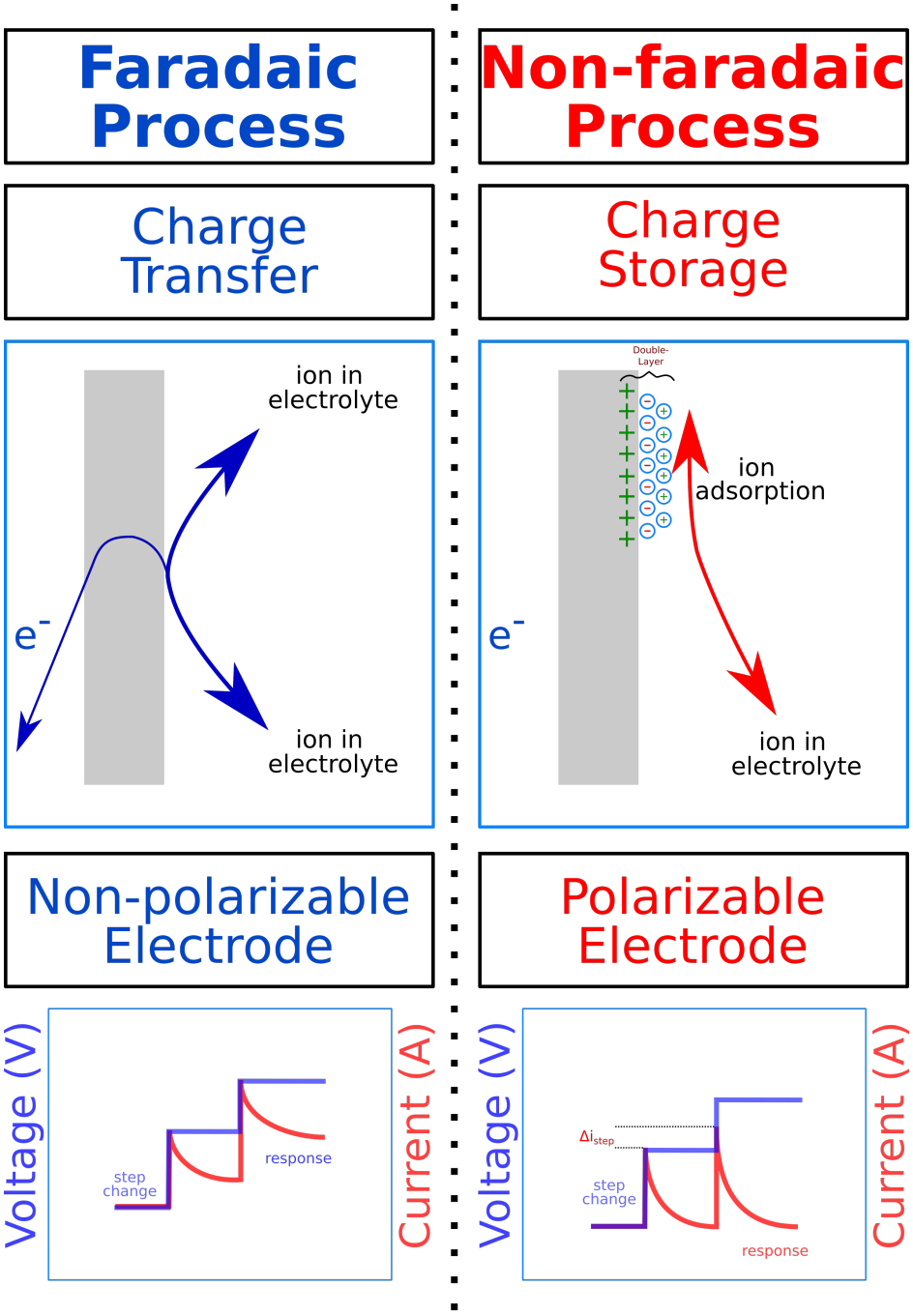

Figure 1.2. Illustration of charge transfer and charge storage for faradaic and non-faradaic processes at the surface of the electrode, respectively. In a predominantly non-polarizable (Faradaic) electrode, a step change in voltage results in an immediate increase of current followed by a slight polarizable (non-Faradaic) change until a new current equilibrates. In polarizable electrodes, a step change in voltage produces an increased current relative to the initial step response before settling to the same equilubrium value as before the step input. The outcome of this increased current amplitude (Δi_{step}) is a gain in stored charge; this is represented as the area under the current response curve.

The following section describes the mechanisms through which charge transfer occurs in bioimplantable electrodes and outlines problems intrinsic to the electrode-electrolyte interface. A brief understanding of the physics of this interface is required to further explore potential solutions. The goal is to understand why introduction of synthetic conductive polymers into this interface will promote decreased interfacial impedance. Ultimately, synthetic conductive polymers allows engineers to manipulate the physical limitations of the electrode-electrolyte interface to promote better charge transfer between electrodes and the electrolyte solution.

1.2.1 Mechanism of Charge Transfer in Neural Interfaces

Ability for current to flow across the electrode-electrolyte interface is a function of Faradaic and non-Faradaic impedance at the electrode surface. This varies depending on the type of current, either direct (DC) or alternating (AC), applied. To understand the means through which current transfers, it is best if we briefly discuss what occurs in the equivalent circuit in both DC and AC cases, respectively.

1.2.1.1 DC Charge Transfer in Equivalent Circuits

In the case of DC charge transfer, the current passed through the circuit will make its way into the solution through the Faradaic impedance resistor, which can be thought of as a purely resistive element referred to as the charge transfer resistance [10]. At the same time, the double-layer capacitance becomes charged to the applied voltage value and remains so until the circuit is either turned off or disconnected. The charging/ discharging rate of the capacitor is reliant on the time constant (τ), a parameter which describes the response to a step input in a linear system. This capacitance can prove to be problematic after the circuit has been disconnected. The charge buildup on the capacitor will begin to leak into the solution at a rate dependent on the time constant of the system. A smaller time constant is indicative of a capacitor that will discharge more quickly, leading to a potentially uncontrolled or unstable environment for the nerve. Furthermore, depending on the capacitance, the stored charge could be large relative to the operating environment of the nerve. Recording electrodes must acknowledge thresholds in the millivolt and nanovolt range; a large buildup of charge will result in an increased susceptibility to

external noise sources [10]. Additionally, recording electrodes must pass enough current to satisfy the bias currents which is impedance dependent.

1.2.1.2 AC Charge Transfer in Equivalent Circuits

In AC charge transfer, the charge is passed through the circuit in an alternating manner. This leads to a charge transfer resistance similar to that of the DC circuit. Unlike the DC circuit an impedance arises at the double-layer, referred to as a constant phase angle impedance, that results from electrode polarization and is described by the empirical relation [10, 19]:

$$Z_{CPA}(\omega) = \frac{1}{(j\omega Q)^n} \tag{1.1}$$

where,

j is an the imaginary number;

ω is the angular frequency $\omega = 2\pi f$;

Q is a measure of magnitude Z_{CPA};

n is a constant ($0 \leq n \leq 1$), representing inhomogeneities in the surface.

In the case where n = 1, Z_{CPA} is represented as purely capacitive and subsequently referred to as the capacitive reactance, where Q is equivalent to the capacitance of the double-layer [10]. It is for this reason why a homogeneous surface is ideal to understand and study electrochemical systems. As previously mentioned, a circuit that contains a small time constant quickly builds up and dissipates charge. This poses a problem when dealing with sensitive tissue in low frequency ranges because the capacitive reactance approaches infinity as the frequency tends to 0. This will result in an infinite impedance, resulting in an unstable environment that is extremely sensitive to motion artifact and succumbs to constant discharging of the chemoelectric potential. That being said, an electrode designed to have a high capacitance can mitigate this low-frequency response.

1.2.2 Types of Electrodes for Recording and Stimulation

The epitome of neuromodulation electrodes is one that prevents leakage from the capacitive double-layer, minimizes interfacial noise, inhibits corrosion, has high charge density, eliminates charge transfer by reducing the charge-resistive boundary, and maintains flexiblity throughout the duration of its use [20–24]. The relationship between electrode material, surface activity, and surface area are all strongly correlated [13]. Specifically, electrodes can be split into two types of ideal electrodes, one is an ideal polarizable electrode, and the other an ideal non-polarizable electrode. Ideal polarizable electrodes behave as a perfect capacitor, minimizing Faradaic current and maximizing displacement current. Non-ideal polarizable electrodes are the opposite, maximizing Faradaic and minimizing non-Faradaic currents. Although a perfect example of each electrode doesn't exist, platinum (Pt) and silver/ silver-chloride (Ag/AgCl) represent an ideal polarizable and an ideal non-polarizable electrode, respectively [25]. Unfortunately, many conventional metal electrodes tend to greatly favor one state over the other. In one study, Riistama and Lekkala observed the characteristics of various polarizable and non-polarizable electrodes over a band of 2-500 Hz, indicating the Pt-electrode rms voltage is greatly reduced when compared to Ag-electodes and that Ag had a higher noise voltage density. Despite Pt polarizability, it readily succumbs to corrosion and therefore should not be used in implantable interfaces [25].

1.2.2.1 Standard Metal Electrodes

Standard metal electrodes, such as stainless-steel (SS), Gold (Au), and Pt are able to effectively conduct electrons in an AC environment, however they prove to be poor materials for biomedical applications. One of the main challenges with bioelectronic interfaces is maintaining a stable communication pathway between the two mediums [26]. Biological material is composed of carbon, is soft and elastic (Young's modulus of cartilage is $0.16x10^6$ Pa), and resides in an aqueous environment [27]. This environment contrasts greatly from the stiffness of metals (Young's modulus of Au and Pt are $79x10^9$ Pa and $0.25x10^9$ Pa, respectively) [27, 28]. The stiffness of metals results from its tightly packed lattice structure. Electron conduction in metals is effective, allowing for electrons to jump between adjacent valence orbitals, however if the valence

shell of an adjacent atom is more than a few angstroms away, this mechanism is no longer viable. Furthermore, the lattice structure of the metals limit their interaction with adjacent electrolytes to electron dense or homogeneous surfaces, tending towards a homogeneous surface (see Fig. 1.1).

1.2.2.2 Intrinsically Conductive Polymers

One method of improving standard metal electrodes is to use synthetic polymers to improve the electrode-electrolyte continuum. Synthetic polymers allow for specified electronic functionality by means of introducing different organic materials, resulting in blends of various organized structures [29]. A synthetic polymer that maintains electrical properties similar to a metal while retaining its polymer chemical structure is referred to as an intrinsically conducting polymer (ICP) [30]. Potential advantages of using ICPs in neuromodulation applications include the ability to fine tune variables such as mechanical properties, ability to conduct ions, electrons and holes, and can be decorated with molecular side groups to improve cell viability [26, 30–33].

Base compounds for ICPs include poly-(para-phenylene), poly(phenylenevinylene), polypyrrole (PPy), polthiophene, polyfuran, poly(heteroaromatic vinylenes), and polyaniline [30]. PPy is has been known to improve charge-pulsing capacity on Pt-wires as compared to bare Pt wires, an improvement on the capacitive nature [32]. Another ICP that has particularly interesting characteristics is Poly(3,4-ethylenedioxythiophere):poly(styrenesulfonate) (PEDOT:PSS) because of its ability to be easily dispersed in water in addition to its relatively affordable price; more importantly, PEDOT:PSS has high mechanical flexibility, excellent thermal, electrochemical and oxidative stability, low band gap, and the means to conduct electrons and ions [29, 32–34]. ICPs obtain their conductive properties through redox doping. Doping can be achieved in one of two ways, either p-type or n-type doping through a chemical or electrochemical process. In p-type doping, partial oxidation leads to a removal of an electron of the carbon (alkene) backbone of ICPs, leading to a hole, causing a delocalization of charges [30]. In n-type doping, partial reduction leads to the addition of an electron in the alkene backbone. Chemical doping processes have been extensively studied, however the current work focus' on electrochemical doping [30, 33, 35, 36].

1.3 Electrochemical Modifications of Standard Metal Electrodes

Standard metal electrodes can be modified with ICPs to improve their charge transfer characteristics. The process through which metal electrodes are coated in an electrochemical process is called electrodeposition. The electrodeposition process occurs when a current is applied to a solution containing a mixture of the ICP in its non-reduced or non-oxidized state. In the case of p-type electrodeposition, an aqueous solution of ICP is prepared and subjected to DC at a potential high enough to allow the Faradaic oxidation to occur at the working electrode.

In this section, I outline the functionality of the electrochemical cell, the mechanisms behind electrodeposition, and subsequent initiation, propagation, and termination of ICPs to modify electrodes. As previously mentioned, the addition of the ICPs will allow for manipulation of the physics at the electrode-electrolyte interface and promote the interconversion of electronic to ionic conduction across the nerve membrane.

1.3.1 The Electrochemical Cell

The electrochemical cell can be described by an equivalent circuit (1.3). This circuit contains a working electrode (where the reaction occurs) and a counter electrode to balance the cells charge. The potential across the cell is monitored by a non-polarizable reference electrode, such as Ag/AgCl, to prevent capacitive buildup which would hinder the ability for adequate reference measurement. When a voltage (potentiostat) or current (galvanostat) is applied across the cell, a reaction may occur. Fig. 1.3 identifies the components of the electrochemical cell. This includes a working electrode where the reaction of interest occurs, a counter electrode that contains a large surface area contact to complete the circuit while preventing participation in the reaction of interest, and reference electrodes to measure the potential across the cell. The reference electrode is positioned in solution, adjacent to the working electrode, which also has its potential recorded via an additional reference.

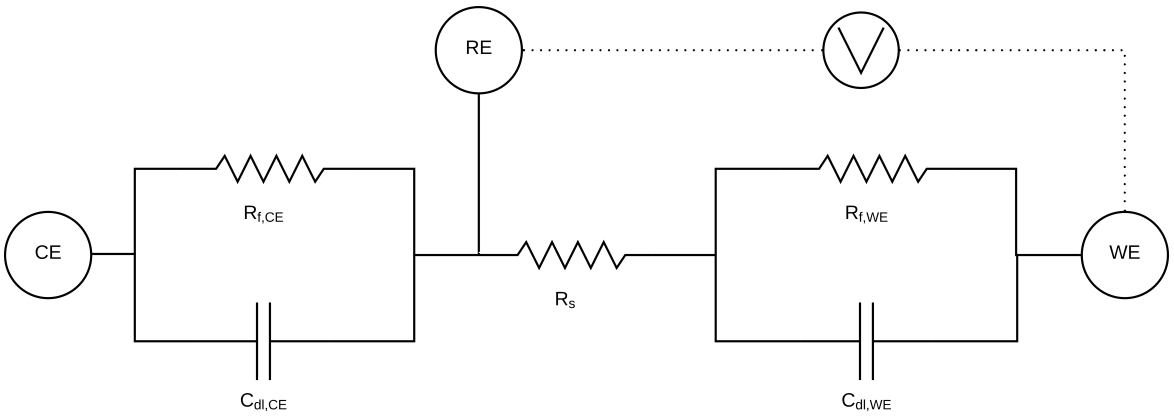

Figure 1.3. Equivalent circuit for the electrochemical cell described in section 1.3. (WE = Working Electrode; RE = Reference Electrode; CE = Counter Electrode).

1.3.2 Electrodeposition of Synthetic Materials

Electrodeposition occurs when a high enough potential is obtained across the electrodes to allow a significant amount of valence electrons to move from the one orbital to the next. This mechanism occurs when a specific thermodynamic chemical potential energy is achieved to catalyze the removal or addition of an electron to induce formation of a radical, leading to a redox polymerization with its neighbor and formation of a product from the reactants that originally began in aqueous solution. As a result of its oxidative or reductive potential, the electrode behaves as a catalyst. In a p-type redox reaction, the products contain a deficit of electrons compared to what it started with, and occurs at the anode of the electrochemical cell. An n-type redox reaction products contain an excess of electrons, and takes place at the cathode. Upon completion, the metallic surface will be coated with the ICP, therefore containing the improved functionality previously described.

1.4 Histology to Study the Physiological Response of Implanted Electrodes

As with all materials that come into contact with biological systems, they have the potential to cause an adverse biological response. In order for bioelectronics to be used clinically, biocompatibility is of utmost concern. In any case, an inflammatory response will lead to tissue encapsulation and subsequent increase in resistance. Grill and Mortimer outlined the inflammatory, bio-incompatible and biocompatible response to subcutaneously placed electrodes in adult cats [37]. Bio-incompatible implants led to an innate immune system response with a significant number of macrophages and foreign body giant cells. In the biocompatible response, a thin, lightly packed layer of fibroblasts, collagen, and macrophages encapsulate the electrode [37]. In any case, resistance at the electrochemical interface increased as a function of the inflammatory response.

Albeit the study by Grill and Mortimer was carried out with subcutaneously place electrodes, the innate environment is similar to a nerve. The nerve is surrounded by various types of collagen, fibroblasts, and can lead to giant cell formation [38–41]. This environment can be qualitatively and quantitatively studied using histology.

1.5 Purpose

Many studies have been performed to alter the surface structure of electrodes. Attempts have been made using carbon-additives, Pt-black, and various types of ICPs [42]. Pt-black and PPy have been successful, however there are polymers that prove to be superior, such as PEDOT:PSS [20, 21]. PEDOT:PSS has greater conductive and oxidative stability than PPy and polyanaline, a particularly high capacitance, and increased conductivity. Furthermore, PEDOT:PSS can incorporate additives, such as carbon black, to increase its mechanical and electrical properties. PEDOT:PSS has been explored in the field of charge-storage, where it was used to improve the galvanic properties of solar cells [34]. Collectively, these properties led to why PEDOT:PSS was potentially advantageous to use compared to other ICPs and conductive materials.

Our lab has used PEDOT:PSS to improve electrodes for neuromodulation. The PEDOT:PSS is synthesized via oxidative electrodeposition, however tends to be fall apart as a result of electrode-nerve shorting and non-uniform current density once a current has been applied in-vivo. There are many methods to deposit this material on conductive surfaces, one of which is through sputtering. We have seen first-hand with CorTec's electrodes the viability of sputtered PEDOT:PSS, and it has been well documented in literature [42–44]. However, sputtering is a process that is not easily performed in laboratories and is expensive due to the necessity of a magnetron sputtering system. Electrodeposition, on the other hand, is a cheap and effective way to alter the surface properties of electrodes via simple electrochemical reactions and is readily available for most laboratories.

In the present, we attempt to modify PEDOT:PSS by suspending mesoporous carbon black (CB) in an aqueous solution containing ethylenedioxythiophene (EDOT) and PSS followed by electrodeposition on a stainless steel electrode. PEDOT in the presence of CB has been studied previously via in-situ chemical oxidative polymerization and layer-by-layer (LbL) assembly, and led to improvements in thermal stability, electrical conductivity, and inhibited the agglomeration of PEDOT [35, 36].We hypothesize that the addition of CB to PEDOT:PSS will lead to a decrease in impedance and improved binding of the ICP to the electrode interface.

Lastly, in addition to modification of PEDOT:PSS, we develop a histology protocol to adequately measure the viability of implanted electrodes. It is desired that the histology protocol will help with identifying biocompatibility, physiological morphology of the nerve, and any possible PEDOT:PSS or PEDOT:PSS/CB that may become dislodged from the surface upon stimulation. Unfortunately, due to circumstances of the 2019 Novel Coronoavirus, chronic and acute animal studies were suspended, meaning electrodes were not implanted.

1.5.1 Thesis Objectives

Aim 1: Explore PEDOT:PSS/CB as a potential new interface as opposed to PEDOT:PSS

Aim 2: Design a histology protocol to analyze peripheral nerve tissue following implantation of conventional electrodes modified with PEDOT:PSS/CB

CHAPTER 2. ELECTRODE DESIGN AND SYNTHETIC CONDUCTIVE POLYMERS

The following work supported the development of methods to coat LUNA probes for work with the Defense Advanced Research Projects Agency (DARPA), LUNA Innovations, and cuff electrodes for our lab's NIH sponsored low-frequency alternating current block (LFACb) project.

2.1 Abstract

The environment neuromodulatory electrodes operate in is extremely complex and delicate. They are in close proximity to tissue that can be easily damaged as a result of mechanical and electrical stressors. Damage may potentially lead to chronic pain, motor dysfunctions, or in the most severe case complete loss of nerve activity. As a result, there is little room for error when designing a safe, biocompatible interface. This chapter intends to provide the reader with a brief introduction to the neuromodulatory mechanism, limitations associate with the electrode-electrolyte interface in neuromodulatory designs, and and a method to decrease interfacial impedance through the addition CB to the ICP PEDOT:PSS. Our lab has explored PEDOT:PSS in the past, however it tends to fall apart during implantation and stimulation; there is a need to develop a more robust interface. This is particularly important during low-frequency alternating current (LFAC) modulation because this mechanism works the electrode more than higher frequency counterparts since currents are slower than the frequency required for double-layer transmission. Cyclic voltammetry (CV) is used to identify surface reactions occurring at the electrode interface during the addition of PEDOT:PSS/CB when electrodepositing; impedance characteristics are then quantitatively analyzed via electrochemical impedance spectroscopy (EIS).

2.2 Potential Solutions to Implantable Electrode Design

In the current section, I briefly reintroduce neuromodulation and the mechanism of nerve conduction. The purpose is to provide the reader a foundation on how electrodes interface with the nerve tissue. Specifically, I attempt to discern the difference between electronic and ionic conduction previously introduced in Chapter 1. The reader should first be able to identify what ionic conduction is and the mechanism through which nerve action potentials are initiated. I then outline problems associated with metal electrodes and how synthetic conductive polymers can be utilized to improve their charge-transfer capabilities at the electrode-electrolyte interface.

2.2.1 Implantable Electrode Design Limitations

Despite the term neuromodulation not being coined until the mid 1960s, its roots were established in the late 18th century by Luigi Galvani. Galvani's work was the foundation to future studies that ultimately led to Hodgkin-Huxley's mathematical description of the initiation and propagation of nerve action potentials. Their work on the giant squid axon brought about the description of how current moves down the axonal membrane. This longitudinal current is a function of the translocation of sodium and potassium ions radially across the axon membrane and the opening and closing of voltage-gated ion channels. Equation 2.1 mathematically describes this relationship between ionic and capacitive current [45]:

$$I = C_M \frac{dV}{dt} + I_i \tag{2.1}$$

where,

I is the total membrane current density;

I_i is the ionic current density (sodium and potassium ions);

V is the membrane potential voltage;

C_M is the membrane capacity per unit area; and

t is time.

Hodgkin knew that in order to properly study flow of ionic current, the voltage gated channels would have to be turned off, and effectively did so through use of a feedback control mechanism known as a voltage clamp, originally introduced by Cole [46, 47]. Had he not used a voltage clamp, channels would not be turned off, and uncontrolled charging and discharging of the voltage-gated networks would occur, diminishing ones ability to study the ionic conduction across the membrane.

Hodgkin-Huxley's experiments were designed for the giant squid axon, which has a diameter of about 1 mm. This is extremely large compared to mammalian axons (can be 20 μm in diameter for humans). Use of the giant squid axon allowed scientists the opportunity to measure voltage changes during an action potential. Without the giant squid axon, it would have been near impossible to measure these changes because of the size of electrodes relative to the size of most nerves. The issue with size of the axon relative to the electrodes used to measure its underlying properties is still an issue today. However, obtaining an electrode small enough to encounter electrical changes in the nerve is no longer the problem thanks to the 21st century manufacturing technology. The present issue is that designers are limited by the physical nature imposed on conductive materials: an increase in impedance as the electrode radii become smaller. This increased impedance arises from the relationship that the conductance of a cylindrical metal electrode is a function of the length of the electrode, internal and outer radii, and conductivity:

$$R = \frac{\rho ln(\frac{r_a}{r_b})}{2\pi L} \tag{2.2}$$

where,

R is the resistance;

ρ is the resistivity;

L is the length; and

r_i is inner (a) and outer (b) radius, respectively.

As stated, electrode size is no longer a physical limitation to prevent them from interacting with the nerve as it is their intrinsic resistance. Unfortunately these high-impedance devices identify more than subtle changes in membrane potential, they begin to pick up on motion and noise artifacts from nearby equipment. The impedance limitation has caused the direction of implantable electrode development to shift from size and mechanical stability to designing for selectivity and reduced impedance at the electrode-electrolyte interface.

2.2.1.1 Charge Transfer Impedance

Impedance in an electrochemical cell is a function of the non-faradaic empirical relationship described in Eq. 1.1. This impedance relationship, referred to as capacitive reactance or reactance, varies as a function of frequency. At high frequencies, the electrode-electrolyte interface becomes almost entirely resistive. However, operation at extremely high frequencies is not ideal in neuromodulation as it may quickly fatigue the targeted fibers. In lower frequency ranges, reactance becomes extremely high for circuits composed of material that is not significantly capacitive at the electrode-electrolyte double-layer.

Our lab has been investigating the use of low-frequency (10 – 50 Hz) alternating current to modulate nerve activity. At these low frequency ranges reactive capacitance can be an issue. The increased reactance leads to increased noise during recording and decreased stability during stimulation. The relationship between potential across the electrode-electrolyte boundary is proportionally related to the current delivered. Therefore, a higher impedance requires a significantly larger potential across the electrode-electrolyte boundary to result in the same amount of current delivery. Increased potential is dangerous when dealing with nerves that operate in potentials on the order of millivolts, as a shorted circuit could permanently damage the targeted fibers. A potential method to improve this electrode-electrolyte interface while retaining mechanical stability is to use ICPs.

2.2.2 Synthetic Conductive Polymers to Improve Implantable Electrodes

Synthetic conductive polymers, also known as ICPs, have gained a lot of traction since the explosion of research that occurred in the early 21st century as a means to improve conventional metal electrodes (i.e., SS, Au, and Pt). ICPs were originally looked at as modifications for supercapacitors and photovoltaic cells. Biomedical and materials engineers took note of these organic materials charge transfer characteristics and began exploring methods to repurpose them for the field of neural engineering. ICPs are able to be tuned using doping techniques similar to those used in the development of semiconductors, allowing for a controlled electrochemical interface that perfectly balances polarizable and non-polarizable electrode designs. Furthermore, similar to the tuning of charge transfer characteristics, ICP material mechanical properties may be altered through use of organic scaffolds, such as carbon nanotubes, or the addition of various additives.

In the present, we attempt to use carbon-black as an additive to the nonpolymerized form of PEDOT, ethylenedioxythiophene, and PSS (EDOT:PSS) solution to prevent the ICP from becoming displaced from the electrode during implantation and subsequent stimulation. Although CB doesn't contain the same 3d-structure as carbon nanotubes, it is our assumption the CB tetrahedron will be incorporated into the PEDOT:PSS matrix upon electrodeposition. It is assumed the graphite-like structure of the conductive carbon (see Fig. 2.3) and will provide support to the underlying PEDOT:PSS structure, improving the durability of the PEDOT:PSS complex and preventing flaking during shearing. CB was chosen as the additive for many reasons, primarily its low-cost and oxidative stability. From an electrical and mechanical standpoint, CB has been proven to improve conductivity, a function of its large surface area, has excellent thermal stability, and the ability to prevent agglomeration of the PEDOT. Furthermore, this material has been previously used in nanoelectronics to improve capacitance and charge transfer characteristics [36, 48–50].

Examination of the addition of CB was performed using electrochemical impedance spectroscopy on PEDOT:PSS/CB electroplated electrodes to determine if the CB was incorporated upon deposition. Cyclic voltammetry is utilized to identify the surface reactions and charge storage behavior of the coated electrodes as a function of CB concentration. As a latent outcome, we further investigate whether or not the CB has a positive or negative effect on overall impedance.

2.3 Electrodeposition of PEDOT:PSS/CB

Ethylenedioxythiphene (EDOT) is an organosulfur moleucule that, upon oxidation, is converted into the conducting polymer PEDOT. The oxidation occurs in two steps, the first of which EDOT is converted into a polaron, forming a tertiary carbocation and a radical. Formation of EDOT radicals via oxidation at the anode initiates the polymerization reaction between adjacent EDOT monomers. Upon further oxidation, a second tertiary carbocation forms. These cations create holes along the PEDOT, such as what is seen in p-type semiconductors, allowing for the transfer of electrons.

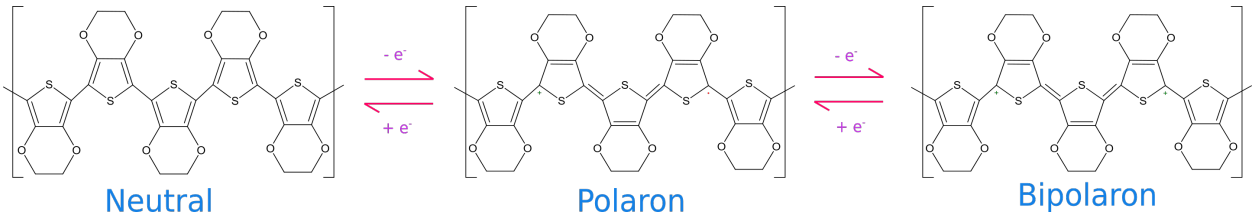

Figure 2.1. Oxidation of neutral PEDOT leads to polaron and bipolaron formation.

One limitation to EDOT is that it is hydrophobic and will not go into solution. PSS, an amphipathic polymer, is typically added to EDOT, lowering the free energy associated with the hydrophobic interaction. Upon addition of EDOT and PSS in solution, the hydrophobic PSS backbone encapsulates the EDOT, creating a cage-like structure with exterior sulfonate ions interacting with the water. As a result, two possible conformations for this caged structure are formed both of which are dependent on the Coulombic and polymer/water interaction. The first is a coiled conformation where EDOT monomers are encapsulated in PSS segments, forming blobs to prevent interaction with water; segments without EDOT are linear to avoid Coulombic repulsions along its anions, creating a conformation referred to as a coiled benzoid [34, 49]. The second conformation results from the linear strings of EDOT-lacking PSS segments, which create a long polymer where EDOT-PSS blobs are separated as much as possible to further reduce Coulombic interactions, creating what was described by Lang as a necklace-like structure [34, 51]. Fig. 2.2 shows the variations in the coiled-benzoid and necklace structures, respectively.

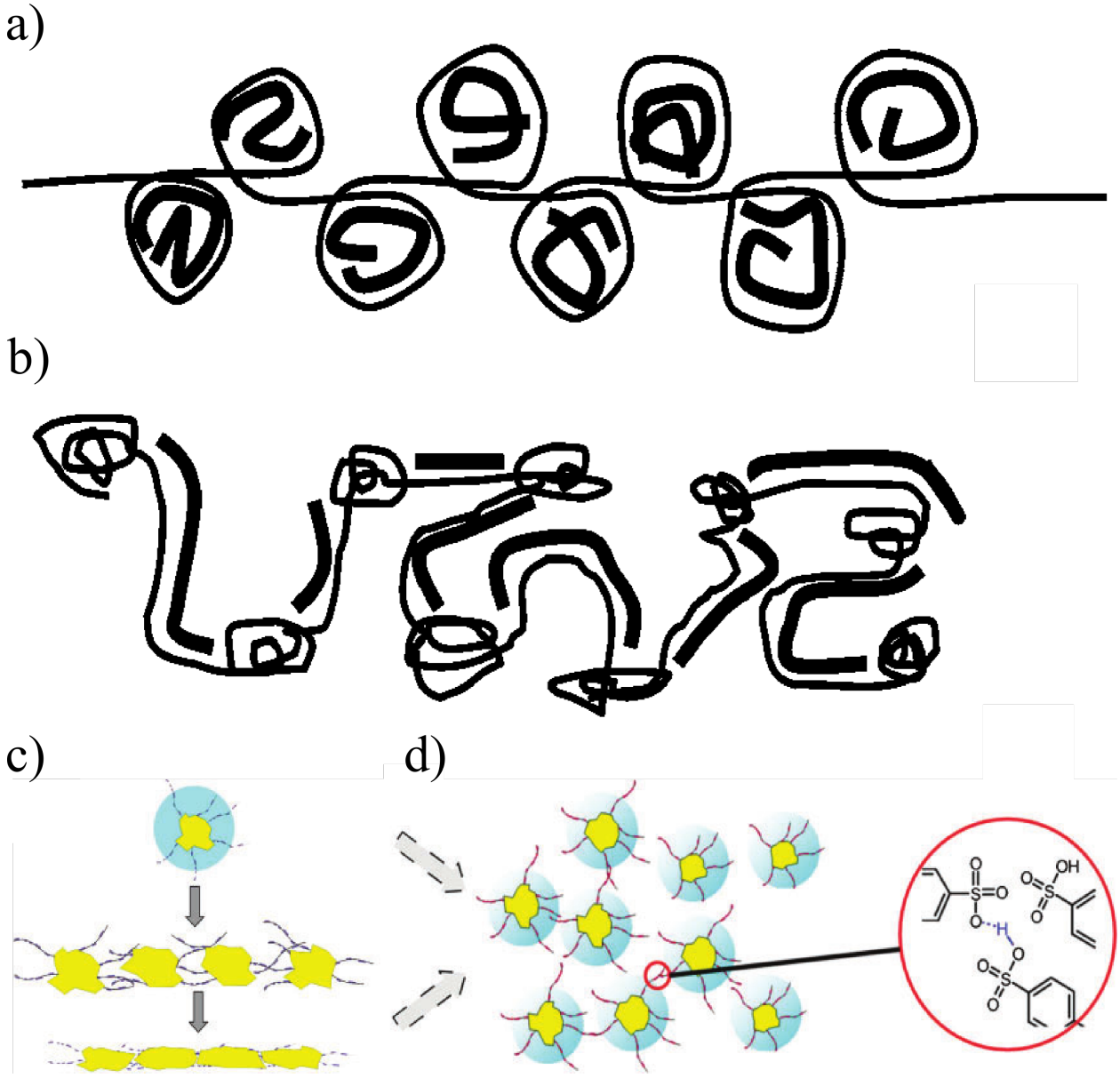

Figure 2.2. In (a) and (b), thin and thick curves represent PSS and PEDOT, respectively. (a) Represents the cage-like structure that occurs when PSS encapsulates PEDOT in solution, referred to as the necklace. (b) A control whereby a cosolvent has been used to impede necklace formation. (c) Layering of the necklace conformation, proposed by Lang et al. (d) Hydrogen bonding interactions between adjacent PSS sulfonic acid groups. Acquired from "PEDOT:PSS films with significantly enhanced conductivity's induced by preferential solvation with cosolvents and their application in polymer photovoltaic cells" and "Microscopical Investigations of PEDOT:PSS Thin Films" with permission. [49, 51]

It is our belief that addition of mesoporous CB to the PEDOT:PSS matrix will result in a similar structure proposed by Xie et al., however chemical oxidative polymerization was utilized in their study as opposed to electrodeposition [35]. Furthermore, due to the inherent conductivity of the carbon, it is likely the addition will reduce overall impedance. Lastly, the carbon may act as a buffer between PSS cages, reducing the Coulombic interaction between adjacent complexes, allowing for a greater density of caged sites on the surface and improved charge density. The carbon-honeycomb (tetrahedron) structure and the PEDOT bipolaron are provided in Fig. 2.3, which depicts the predicted relationship formed on the surface of the electrode upon addition of CB.

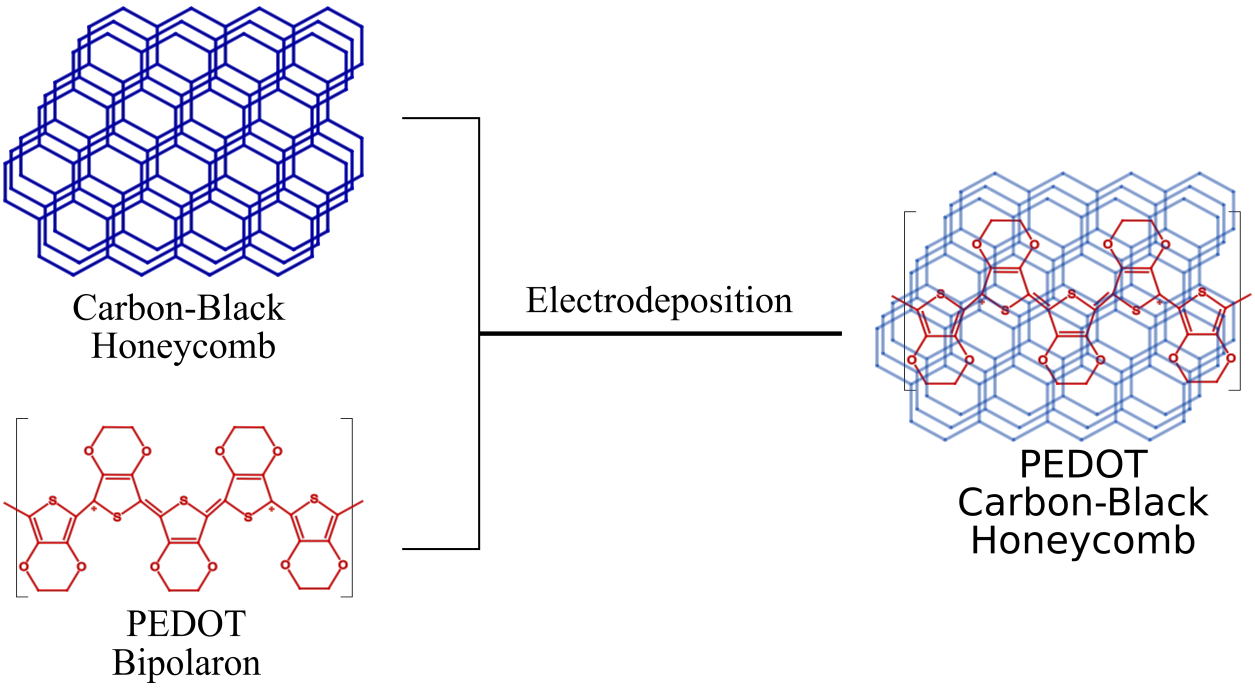

Figure 2.3. Proposed PEDOT:PSS/CB structure formed through the addition of carbon-black and PEDOT at the anode during electrodeposition.

2.4 Quantitative Assessments of ICPs

Quantitative assessments of the electrode surface following deposition is essential to determining whether the predicted hypothesis was a success. In this section, I describe cyclic voltammetry and electrochemical impedance spectroscopy as quantitative methods used to analyze if electrochemical deposition followed by polymerization of ICP is occurring during the coating process and whether or not the effective impedance of the solution has changed.

2.4.1 Cyclic Voltammetry

Cyclic voltammetry (CV) is a technique used to explore the Faradaic effects in an electrochemical environment, and occurs when an electrochemical cell is at a potential magnitude that exceeds those predicted by the Nernst equation (see Eq. 2.3). CV is extremely useful in analyzing redox reactions that occur on the surface of the electrode and bulk media, such as the oxidation of PEDOT:PSS. The setup for a CV is a three-point measurement technique whereby a working electrode contains the material under study and sits opposite from the counter electrode, a high surface area electrode that does not participate in the CV reaction, having the primary role of the current return. A reference electrode is affixed to the working electrode, and a second reference electrode is situated in the electrolyte solution some distance away from the working and counter electrodes (resembles the setup shown in Fig. 1.3). This second reference electrode is an inert, ideally non-polarizeable electrode that does not contribute to the reaction at the surface of the working electrode. Subsequently, a potential difference related to the half-cell potential of the reference electrode in the electrolyte solution, in addition to the voltage drop across the working and counter electrodes, may be recorded from the two reference electrodes.

$$E = E^{\circ} - \frac{RT}{nF} ln(Q) \tag{2.3}$$

where,

E is the cell potential;

E° is the standard cell potential;

n is the number of electrons transferred in the reaction;

F is the Faraday constant (96,500 C/mol);

R is the ideal gas constant (8.314 J/mol-K); and

Q is the reaction quotient.

2.4.2 Electrochemical Impedance Spectroscopy

Rapid electrochemical impedance spectroscopy (EIS) is a technique used to characterize the response of electrochemical systems. The rapid EIS technqiue was developed in our lab by David Sempsrott to test impedance in the 10 Hz to 50 kHz range [52]. This technique is done using a two-point measurement system and can be applied for a number of reasons, such as evaluating coatings post electrodeposition, understanding the deposition mechanisms, and outlining the synthesis of organic material via the use of electric potential to achieve an activation energy that initiates a surface reaction. Rapid EIS is a quick and effective approach to the typical EIS technique, which can be time consuming and only utilizes specified frequency ranges as opposed to the large spectrum. The downside to using the rapid technique is the incongruities that arise at frequencies below 10 Hz, as these frequencies take longer time to properly sample. The duration of our rapid EIS measurements are in fact, rapid (tested anywhere between 10 and 40 seconds), and therefore frequency response below 10 Hz is inconsistent.

Evaluation of the equivalent circuit is typically performed using a Z-arc Cole-Cole plot (see Fig. 2.4), which can be obtained from testing large ranges of frequencies and plotting their resulting reactivity against the real component of impedance (resistance). At high frequencies, this relationship provides the resistance of the solution, and at low frequencies the resistance of the electrode and electrolyte solution. Additionally, the angle tangent to the impedance plot at R_∞ provides the constant-phase element, which describes the double-layer capacitance. A large angle, correlating to a greater phase, indicates there is a substantial capacitive component at the electrode-electrolyte interface. These relationships, which describes the equivalent circuit in Fig. 1.1, may be expressed mathematically using the following relationship [53]:

$$Z(\omega) = R_\infty + \frac{R_0 - R_\infty}{1 + (j\omega\tau_Z)^\alpha} \tag{2.4}$$

where,

Z is the complex impedance;

ω is the angular frequency;

R_∞ is the resistance at very high frequencies;

R_0 is the resistance at very low frequencies;

τ_Z is the characteristic time constant of the system, corresponding to a characteristic angular frequency, $\omega_Z = 1 / \tau_Z$;

α is a measure of the constant phase element (ϕ_{CPE}), $\alpha = \phi_{CPE} / 90^\circ$; and

j is the imaginary number.

In the present, we would like to minimize the capacitive reactance as much as possible to mitigate potential impedance arising from a charging and discharging capacitor. This can be viewed as a decrease in the magnitude of the y-axis on the Cole-Cole plot, and a decrease in magnitude of impedance and removal of the phase element in a Bode plot, which describes the frequency response of the system.

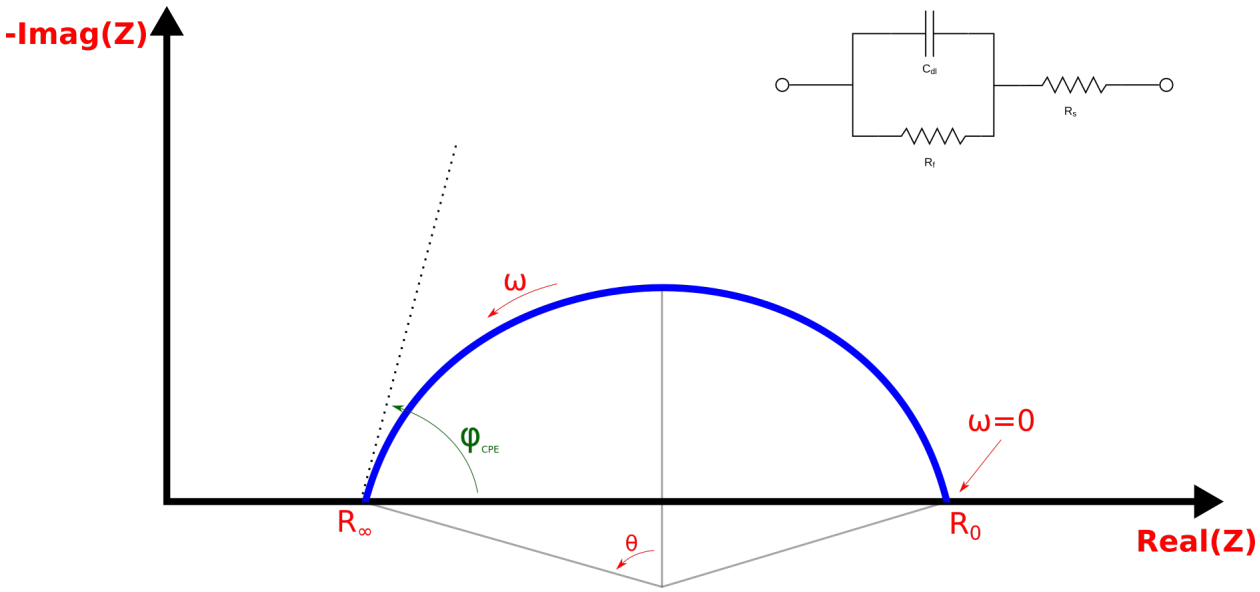

Figure 2.4. Z-arc Cole-Cole Plot. At low frequencies ($\omega = 0$), the solution beings to approach its DC resistance (R_0), which is defined as the resistance of the electrode and electrolyte. When frequency increases, reactive capacitance also increases. Impedance is at a maximum when the reactive capacitance of the electrode-electrolyte plateaus. As the frequency approaches infinity ($\omega = \infty$), the impedance approaches the electrolyte (R_∞) due to the capacitor shorting at high frequencies. The angle tangent to the Real(Z)-axis of the Z-arc Cole-Cole provides the constant-phase element, modeling the behavior of the double-layer which is an imperfect capacitor. Pictured in the upper right corner is the equivalent circuit that may be described by this relationship.

2.5 Methods

2.5.1 Fabrication of Electrodes for Electropdeposition

Electrodes are designed using a 25G (0.52 mm OD) needle (BP PrecisionGlide) and a 15 mm segment of CoonerWire (AS632; 0.3 mm OD). Needles are roughened using a piece of sandpaper to remove any surface oxides and subsequently sectioned into 3 mm segments. A 1 mm section of CoonerWire, roughly 5 mm from one of the ends, is stripped of its Teflon coating to expose the underlying stainless-steel wire. The wire is then carefully inserted into the well of a 3 mm segment of the 25 G needle until the exposed section of the wire is in-line with the needle and thereupon crimped to create contact between the two surfaces. A 2 mm section on the unaltered end of the CoonerWire is then removed to expose the wire. Electrical continuity between the exposed end of the wire and the needle is then confirmed using a multimeter. Thereafter, the electrode is stored in a vial that has had its air displaced with nitrogen to prevent surface oxidation. Fig. 2.5 depicts the 3 mm segment of the 25 G needle crimped onto the CoonerWire.

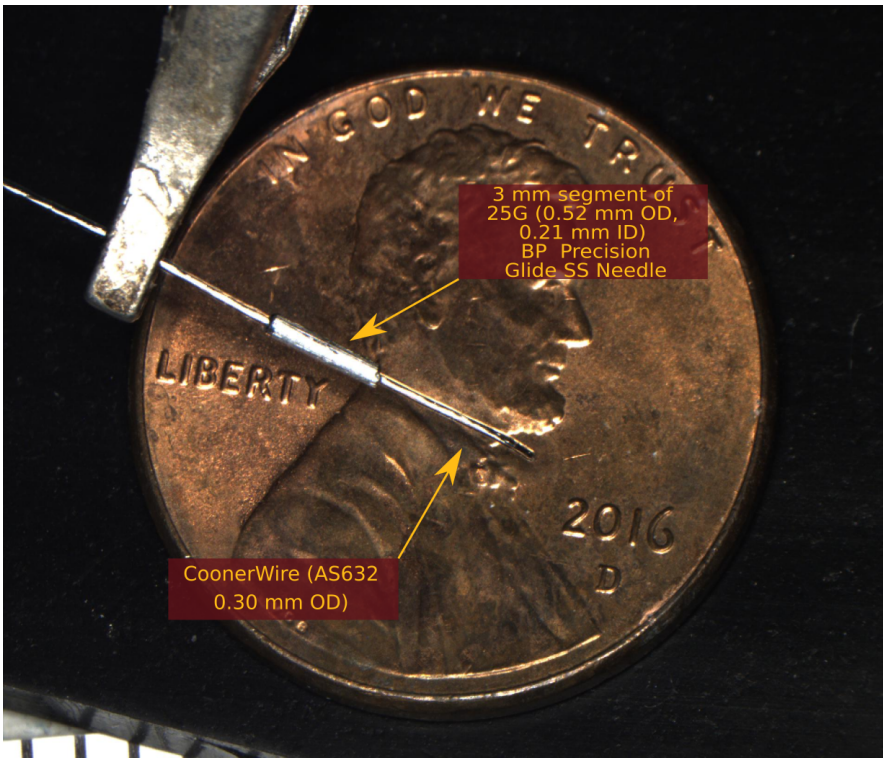

Figure 2.5. Electrode used during electrodeposition of PEDOT:PSS/CB.

2.5.2 Preparation of PEDOT:PSS and PEDOT:PSS/CB Suspension

At the beginning of every week, seven 20 mL 20% (v/v) ethanol/ double-deionized H2O (EtOH/$_{dd}H_2O$) solutions were prepared. Six of the samples contained an EDOT:PSS (v/v) ratio of 0.4, a value chosen based on a study by Horii et al. [54]. The concentrations of EDOT and PSS within these samples were 3.33 mg/mL and 6.94 mg/mL, respectively. PSS was added to the EtOH/$_{dd}H_2O$ solution before the EDOT monomer to prevent agglomeration. Immediately following addition of the EDOT:PSS, various concentrations of CB was added to each respective sample (0, 1.0, 2.0, 0.10, 0.05, and 0.01 mg/mL, respectively). Mixing occurred in a similar manner to Xie et al., whereby N_2 was bubbled through the solution during sonication to minimize the presence of oxygen. Sonication occurred for 30 minutes before the vials were sealed and stored in a refrigerator at 4 $^{\circ}C$ until they were ready to be used. An additional seventh, negative control sample was prepared using similar techniques with the absence of the EDOT monomer and subjected to a CB concentration of 1 mg/mL.

2.5.3 Electrochemical Impedance Spectroscopy

Rapid EIS was performed on the SS electrodes prior to CV and electroplating, and again immediately following electrodeposition of the material. A two-point technique was used to characterize the impedance of the electrode. A function generator (HP 33120A) was used to produce a noise source that would be passed through an amplifier (Tektronix's AM 502) to act as the AC input to a voltage-controlled current. The current source was then passed through an electrochemical interface (Solartron SL 1287) to initiate galvanostic EIS measurements. Voltage differences on the working and counter electrodes were passed into a two-channel compact filter/amplifier (Precision Filters Inc. PFA-2) and digitized using a data acquisition (DAQ) device (National Instruments BNC2090A and USB-6361) at a sampling rate of 500 kHz. Data was then processed in MATLAB (2019a, Mathworks Natick, MA). A second EIS was performed immediately following electroplating. Frequencies were tested in the range of 0.1 Hz to 10 kHz and subsequently plotted using Bode and Cole-Cole diagrams. Lastly, Bode data and Cole-Cole

data were analyzed using methods described in [52]. The auxillary (counter) electrode has a surface area much larger than the working electrode to ensure the half-reaction does not limit the process at the working electrode; a result of a low current density from a larger electrode.

2.5.4 Cyclic Voltammetry

CV measurements were made using a function generator and an electrochemical interface. The function generator was set to triangular waveforms at a frequency of 100 mHz and amplitude of 3 volts peak-to-peak (V_{pp}). Ramping occurred negatively from 1.5 V to -1.5 V. A Ag/AgCl reference electrode was used as the standard for all CV experiments. Voltage and current signals were passed into a data acquisition device and sampled at a rate of 2 kHz. Sampling occurred for approximately 5 minutes, however only 10 consecutive cycles (approximately 130 seconds) underwent processing in MATLAB.

2.5.5 Electrodeposition of PEDOT:PSS

The SS electrode to be coated acted as the working electrode and was placed in a the solution under study (either PEDOT:PSS, PEDOT:PSS/CB, or CB/PSS). All measurements were made in the presence of Ag/AgCl reference electrode and a carbon rod counter electrode. Electrodeposition was tested in two different scenarios. Scenario #1 included running the elctrochemical cell potentiostatically at a DC voltage of +1 V for 20 minutes. In scenario #2, the cell was run under galvanostatic conditions at +200 uA for 5 minutes. Electrodeposition current and voltage readouts were sent to a data acquisition unit and sampled at 2 kHz before being analyzed in MATLAB. Following the length of the depositing period, electrodes were removed from the solution and qualitatively analyzed by acknowledging whether a color change occurred on the surface of the electrode, which acted as a visual indicator for whether or not a reaction took place on its surface.

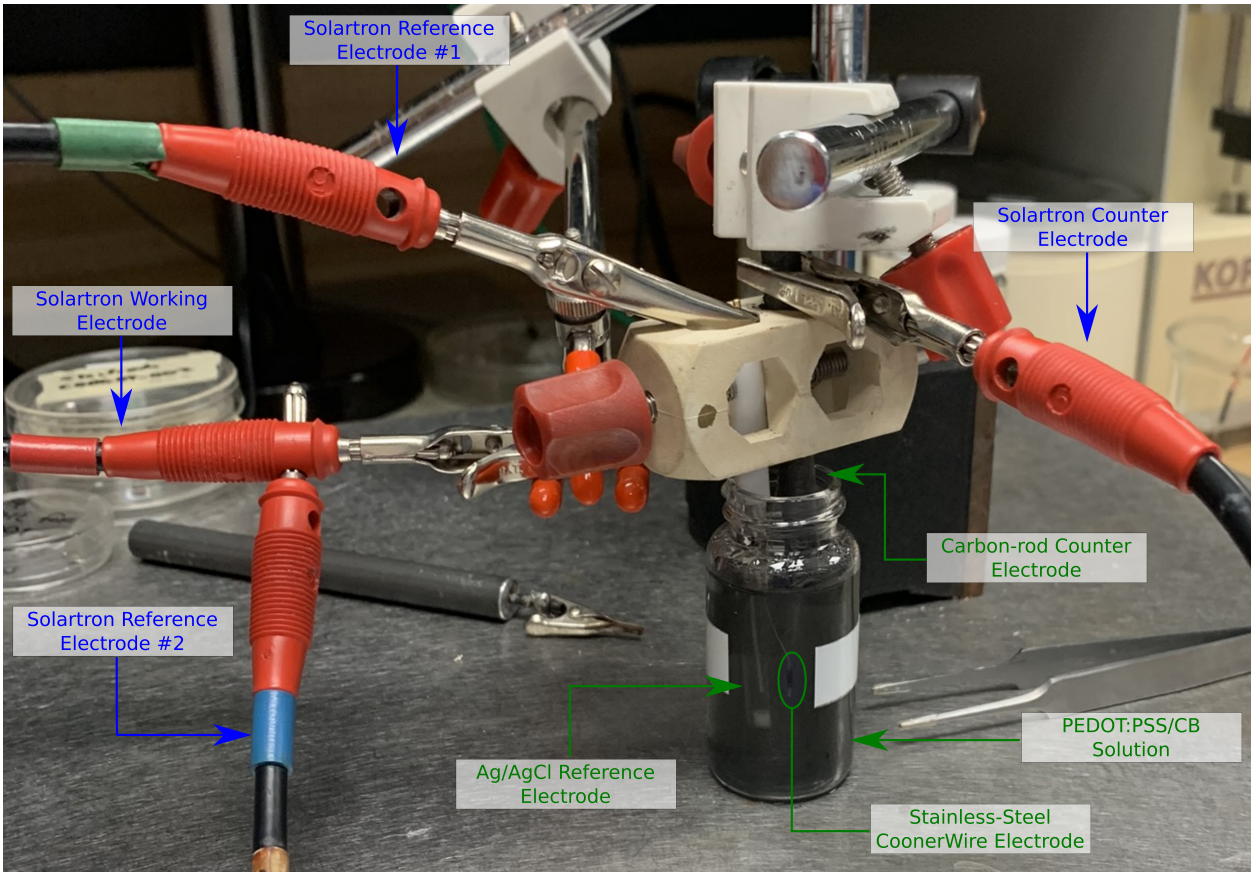

Figure 2.6. Electrodeposition and cyclic voltammetry station setup. The solartron reference electrodes were attached on the Ag/AgCl and stainless-steel CoonerWire electrode, respectively. The counter (auxillary) electrode was affixed to the carbon-rod which was submerged in solution adjacent to the Ag/AgCl reference electrode and stainless-steel CoonerWire electrode (working electrode).

2.5.6 Sample Coating Groups for Electrodeposition

Electrodes were grouped based on the week that the PEDOT:PSS or PEDOT:PSS/CB suspension was made. Electrodes were assigned a coating solution that contained a set CB concentration. In the case of the bare electrodes, no PEDOT:PSS or PEDOT:PSS/CB concentration was included; samples were tested in the same phosphate buffer saline (PBS) solution. Ideally, samples made each week contained a similar concentration as the week before, thus providing an increased sample size and redundancy. Tables 2.1, 2.2, 2.3 identifies electrodes and their electrodeposited solution, solution concentration, and duration of coating.

Table 2.1. Group C00601; 1 M HCl-soaked Stainless-steel electrodes ($t_{soaked} \approx 60$ min.); $T_{coating}$ = 20 min.

Electrode Number	Coating Solution	[EDOT] (mg/mL)	[PSS] (mg/mL)	EDOT:PSS (v/v)	[CB] (mg/mL)
C00603_001	C00601_001	3.33	6.94	0.4	0
C00603_002	C00601_001	3.33	6.94	0.4	0
C00603_004	C00601_002	3.33	6.94	0.4	1
C00603_005	C00601_003	3.33	6.94	0.4	2
C00603_006	C00601_004	3.33	6.94	0.4	0.5
C00603_007	C00601_005	3.33	6.94	0.4	0.1

Table 2.2. Group C00609; $T_{coating}$ = 20 min.

Electrode Number	Coating Solution	[EDOT] (mg/mL)	[PSS] (mg/mL)	EDOT:PSS (v/v)	[CB] (mg/mL)
C00609_001	C00608_001	3.33	6.94	0.4	0
C00609_002	C00608_001	3.33	6.94	0.4	0
C00609_003	C00608_001	3.33	6.94	0.4	0
C00609_004	C00608_002	0	6.94	0	1
C00609_005	C00608_003	3.33	6.94	0.4	1
C00609_006	C00608_004	3.33	6.94	0.4	2
C00609_007	C00608_005	3.33	6.94	0.4	0.1
C00609_008	C00608_006	3.33	6.94	0.4	0.05
C00609_009	C00608_007	3.33	6.94	0.4	0.01
C00609_010	C00608_00	3.33	6.94	0.4	0.01
C00609_012	C00608_005	3.33	6.94	0.4	0.1

Table 2.3. Group C00623; $T_{coating}$ = 5 min.

Electrode Number	Coating Solution	[EDOT] (mg/mL)	[PSS] (mg/mL)	EDOT:PSS (v/v)	[CB] (mg/mL)
C00623_002	C00623_002	0	6.94	0	1
C00623_003	C00623_003	3.33	6.94	0.4	1
C00623_004	C00623_004	3.33	6.94	0.4	2
C00623_005	C00623_005	3.33	6.94	0.4	0.1
C00623_006	C00623_002	0	6.94	0	1
C00623_007	C00623_006	3.33	6.94	0.4	0.05
C00623_008	C00623_007	3.33	6.94	0.4	0.01

Table 2.4. Group C00706; bright and sanded (1200 GRIT $\rightarrow$ 400 GRIT $\rightarrow$ EtOH rinse).

Electrode Number	Coating Solution	Bright / Sanded
C00706_001	Saline	Bright
C00706_002	Saline	Bright
C00706_003	Saline	Bright
C00706_004	Saline	Bright
C00706_005	Saline	Bright
C00706_006	Saline	Bright
C00706_007	Saline	Sanded
C00706_008	Saline	Sanded
C00706_009	Saline	Sanded
C00706_010	Saline	Sanded
C00706_011	Saline	Sanded
C00706_012	Saline	Sanded

2.6 Results

2.6.1 Cyclic Voltammetry

CV measurements indicated that there was oxidation reaction occurring on the surface of the electrodes in both the PEDOT:PSS and PEDOT:PSS/CB cases, a result of the ICP deposition. In Fig. 2.7 are two oxidative CV peaks. As previously mentioned, when PEDOT moves away from its neutral state, it forms a polaron; further oxidation will lead to the formation of a bipolaron. The two characteristic peaks are the result of the formation of these polarons. At higher potentials, a bipolaron formation occurs. Fig. 2.7 shows how PEDOT:PSS and PEDOT:PSS/CB curves vary between the two cases; addition of CB caused a significant reduction in area of the CV curve. In both cases, CV charge capacity changes as a function of time (increasing cycles), further contributing to the evidence of electrochemical modification.

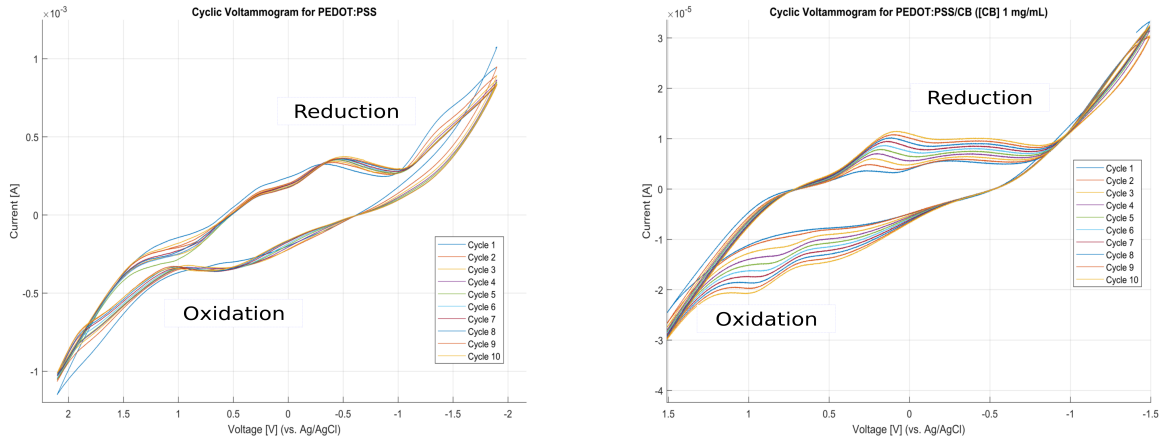

Figure 2.7. Cyclic voltammogram, using US convention, for both PEDOT:PSS and PEDOT:PSS/CB cases. In this figure, negative current correlates to oxidative current and positive current relates to reductive current. The addition of CB to the matrix had a significant impact on the area under the CV curve, greatly diminishing it. The positive (negative) current peaks indicate that there is a redox reaction taking place on the surface of the electrode, relating to the deposition and polymerization of PEDOT:PSS on its surface (Ramping occurred at 100 mV/s).

CV was performed on SS control samples to identify a baseline for the electrodes used during coating. Fig. 2.8 shows the voltammogram for bare electrodes adjacent to PEDOT:PSS/CB electrodes coated with increasing concentrations of CB in saline. The bright electrode has the largest charge capacity, followed by the sanded and "- control" case, which had the smallest charge capacity. The negative control was an electrode plated in the absence of PEDOT with 1 mg/mL of CB. When comparing the samples to the PEDOT:PSS and PEDOT:PSS/CB cases, there is a significant increase in the charge capacity of the coated electrodes. Charge capacity was inversely proportional to CB concentration, with pure PEDOT:PSS containing the greatest charge capacity. Voltammograms of the saline solution lacked the characteristics found in the PEDOT:PSS/CB coating solutions, missing oxidation and reduction peaks that matched those of the coating solutions. Despite these differences, in both solutions the electrode that has the least amount of CB in its matrix had the greatest charge capacity. This can be see in Fig. 2.7, where the PEDOT:PSS curve is of significantly greater area than the PEDOT:PSS/CB curve containing 1 mg/mL carbon black in solution. Therefore, addition of CB leads to a reduction in charge capacity.

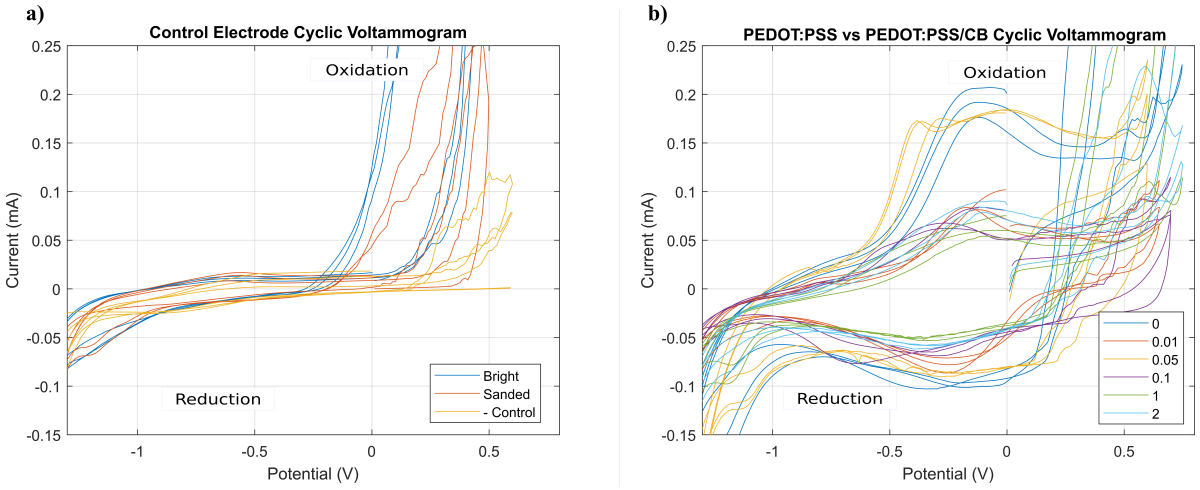

Figure 2.8. Cyclic voltammograms, using IUPAC convention, of control electrodes and various concentrations of PEDOT:PSS/CB in saline. CV in saline provides the polarizable offset. (a) Charge capacity is significantly greater in the bright control electrode, followed by the sanded and "- control" cases, respectively. (b) Charge capacity was inversely related to CB concentration (legend is in units of mg/mL), identified through the increase in oxidative (positive) and reductive (negative) current. The PEDOT:PSS sample, containing no CB, had the greatest charge capacity. (Ramping occurred at 25 mV/s).

2.6.2 Electrochemical Impedance Spectroscopy

Addition of CB to the PEDOT:PSS ICP matrix greatly reduced the impedance of the conductive polymer at frequencies above 100 Hz. CB concentrations above 1 mg/mL significantly reduced impedance relative to those below 1 mg/mL. In low frequencies, PEDOT samples appear to be less capacitive; however, at higher frequencies the CB additive provides a greater and more abrupt attenuation in both impedance and phase elements. This is confirmed in Fig. 2.9, whereby increased CB concentration led to a greater loss in impedance and positive gain in phase. Bode plot (Fig. 2.9a) indicates how at low frequencies (less than 0.1 Hz), the CB-lacking samples attained a more substantial decrease in phase until about 1 to 10 Hz. This decrease is greatest in samples that contain 1 and 2 mg/mL CB; samples that are less than this appear to have similar phases seen by the PEDOT:PSS and bright surfaces. In Bode plot (Fig. 2.9c), there is no sample containing pure PEDOT:PSS, however it is evident that there is a similar trend to (Fig. 2.9a), where a decreased amount of CB leads to a similar response to a PEDOT:PSS-coated electrode. In both cases, samples that had 2 mg/mL CB resulted in a significant decrease in impedance, with the R_∞ approaching 100 Ohms rather quickly.

Cole-Cole analysis provides a quick insight into the capacitive nature of the coated electrodes. PEDOT:PSS and PEDOT:PSS/CB significantly reduces the capacitive elements of the electrode, which can be corroborated with the phase results shown in the adjacent Bode plot. Samples that had a CB concentration of 2 mg/mL appeared to be the least capacitive. As the concentration decreased, capacitive elements increased. In Fig. 2.9b, the samples containing 0.10, 0.05, and 0.01 mg/mL CB tend to approach similar complex response ($\omega = \infty$) that is seen in the PEDOT:PSS-only samples. PEDOT:PSS and bright or sanded uncoated surfaces are similar in their capacitive elements, as indicated by the nearly linear Cole-Cole response in the two samples; in both cases, the R_0 is not viewable within the real-axis limits of the graph. This is not the case for samples containing more than 1 mg/mL CB, as they have an R_0 that appears to reside below 200 Ohms (see Fig. 2.9b and Fig. 2.9d). In all cases, increased CB concentration led to a lowering of the high corner frequency, potentially arising from an increase in the surface area as a result of CB addition.

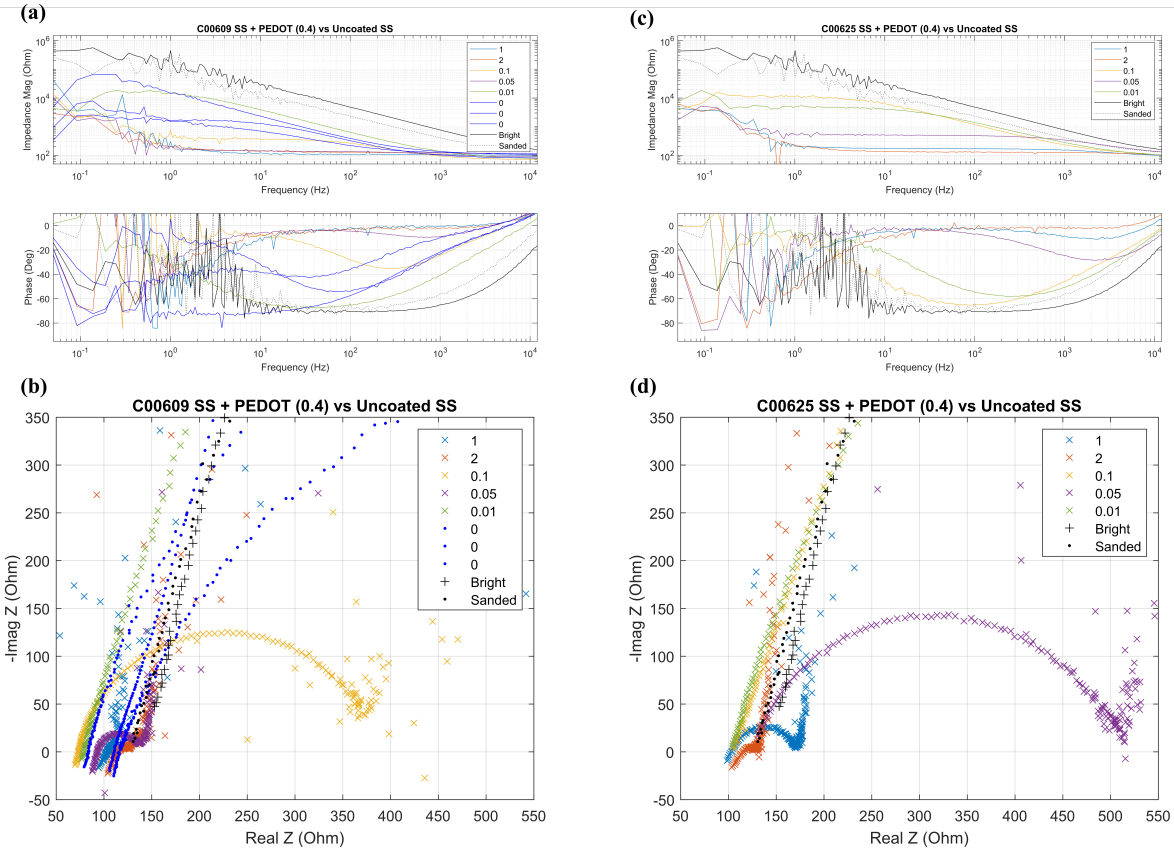

Figure 2.9. The addition of CB to PEDOT:PSS resulted in a significant decrease in the overall impedance of electrodes. Larger CB concentrations correlated to a greater decrease in impedance, with concentrations larger than 1 mg/mL having significant outcomes.

Impedance of various PEDOT:PSS/CB samples as a response to frequency can be viewed in Fig. 2.10. Fig. 2.10a shows the impedance as a function of frequency ranging from approximately 0.01 Hz to 10 kHz. In the extremely low frequency ranges, PEDOT:PSS has an overall lower impedance than the samples modified with CB (Fig. 2.10a). However, as the impedance increases, PEDOT:PSS samples impedance reduces at a much smaller rate than the samples modified with CB (Fig. 2.10c). At a frequency around 1 Hz, PEDOT:PSS/CB is already approaching its R_∞ of 100 Ohms. This indicates that the CB modified PEDOT:PSS samples may be more effective in this frequency range than the unmodified PEDOT:PSS. The variations of R_∞ for both samples is a result of the electrode size variations.

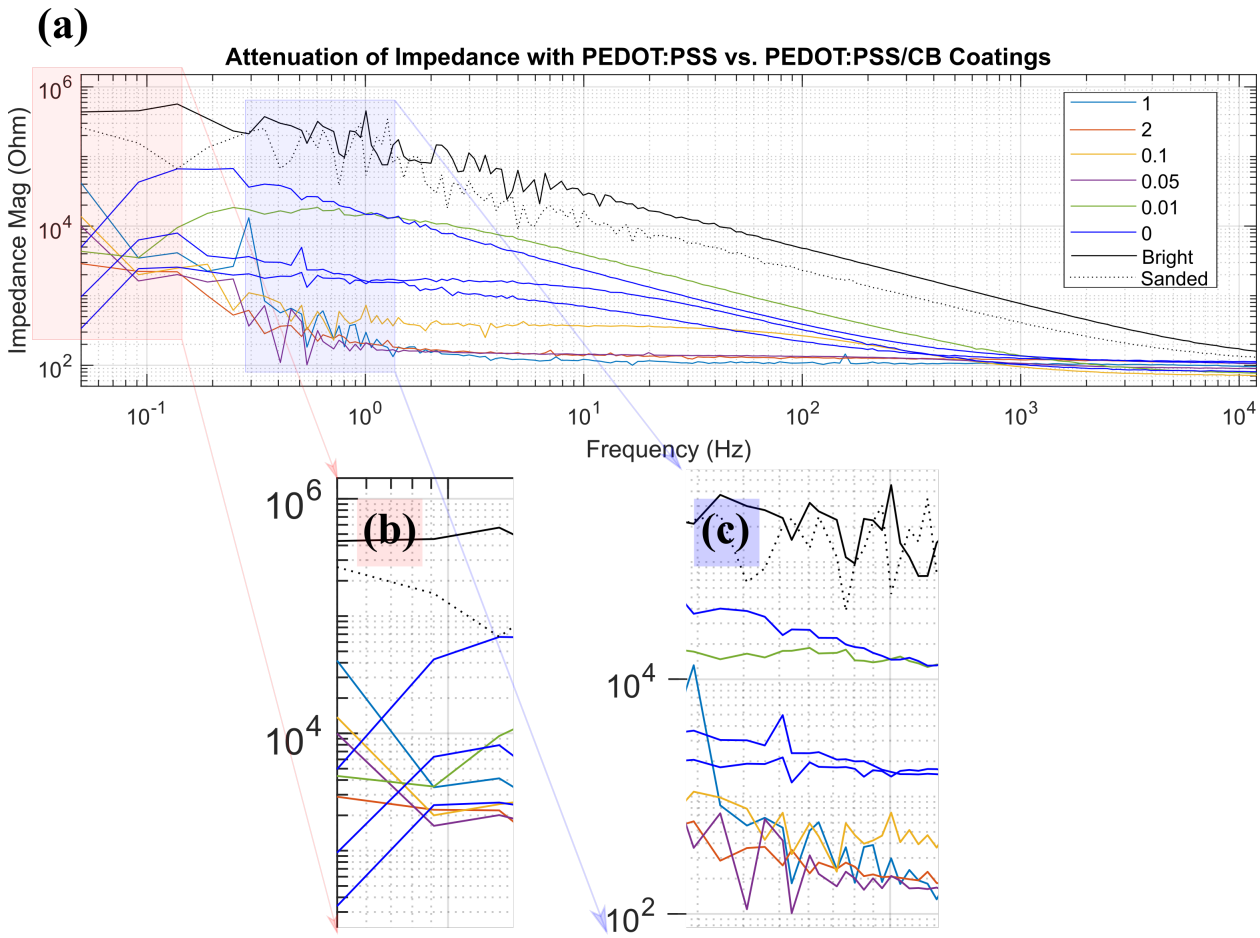

Figure 2.10. (a) Overall impedance response to rapid EIS. (b) Effect of PEDOT:PSS/CB concentration and impedance in low frequency ranges. Samples coated with CB in the low-mid frequency ranges tend to behave poorly compared to PEDOT:PSS; (c) however, at frequency ranges from 1 Hz onward, PEDOT:PSS/CB impedance is significantly reduced compared to the PEDOT:PSS counterparts. Samples containing fractional amounts of CB (green), show characteristics dominated by PEDOT:PSS.

In a separate study, electrode size and surface roughness were looked at to determine if they would have a significant impact on the starting impedance for samples (see Fig. 2.11). Bright stainless-steel electrodes were predominantly capacitive until reaching about 1000 Hz. For the range of electrode sizes listed, impedance measurements indicated size did not significantly affect the outcome in the bright cases. This contrasts from the sanded stainless-steel electrodes, which appeared to have lost some of their capacitive nature in result to surface roughness. These electrodes saw an immediate fractional decrease in overall impedance, with larger surface areas favoring a greater decrease across all frequency ranges. In both scenarios, electrodes approach an R_∞ of approximately 100 Ohms. Results were averaged for both the bright and sanded cases and used as controls for the coating of PEDOT:PSS/CB; averages appear in the bottom graph in Fig. 2.11.

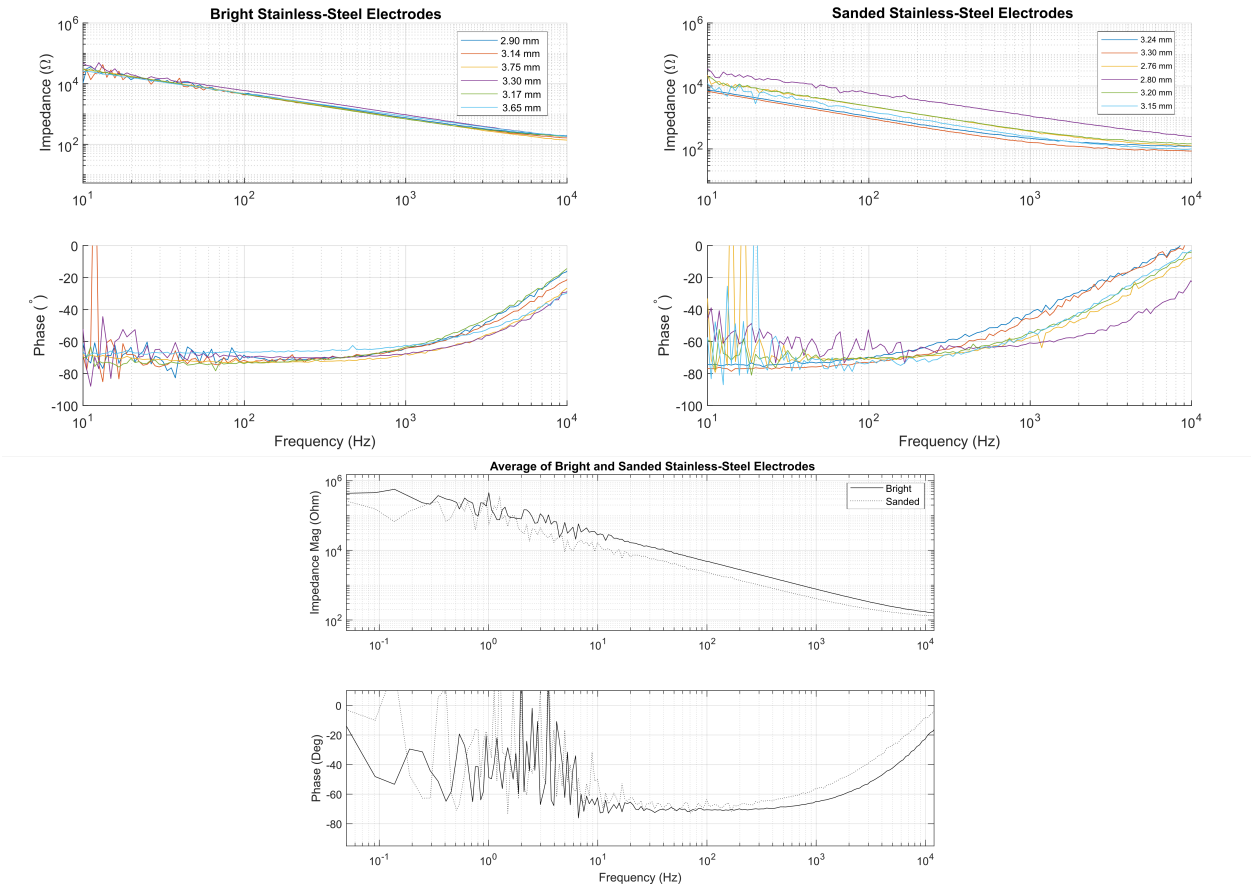

Figure 2.11. Bright and sanded stainless-steel impedance cases. Results were used to determine variance between size and impedance across the frequency ranges used during rapid EIS of PEDOT:PSS and PEDOT:PSS/CB samples.

At one point in the study, electrodes were accidentally soaked in HCl prior to being submerged into the PEDOT:PSS/CB solution for coating. The results were not consistent with the aforementioned. The HCl acts as an oxidizing agent, oxidizing the surface of the SS electrode, hindering its ability to effectively coat. There was no time constraint for HCl-soaking, however they were generally allowed to soak for an hour prior to submitting them to the coating solution for electrodeposition. There was an electrode that was allowed to soak in 1 M HCl over the weekend (approximately 48 hours), causing the solution to turn blue and corrosion of the material, completely destroying the electrode. In Fig. 2.12, these results indicate that there is a loss of relationship between the concentration of CB and the ability to reduce impedance upon coating.

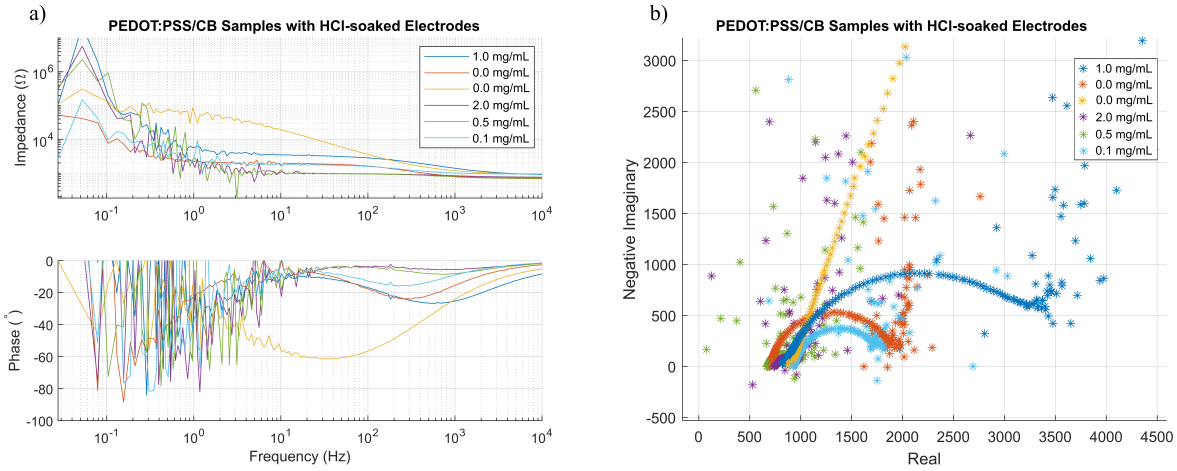

Figure 2.12. Electrodes were mistakenly soaked in 1 M HCl for approximately one hour before being used in electrodeposition experiments. Corrosion of the material led to random EIS results, contrasting from previous results indicating CB concentration was inversely related to impedance.

CHAPTER 3. HISTOLOGY OF THE PERIPHERAL NERVE

The following work supported deliverables for our work with the Defense Advanced Research Projects Agency (DARPA) and LUNA Innovations in addition to a new journal publication that calculated the permittivity of the perinuerium. I would like to give a special thanks to Dr. Carol Bain, DVM, HTL (ASCP^{cm}) from the Indiana University School of Medicine for her guidance in developing processing and staining techniques.

3.1 Abstract

The study of biological tissue and its underlying structural properties is known as histology. Possessing a means of measuring the host-response as well as the morphology of tissue subjected to bioimplantation is critical to the success of developing bioimplantable technologies and preservation of the neuron [55–57]. Histology plays a crucial role in the study of normal cellular function and its subsequent changes as a result of disease and foreign body invasion. At the cellular level, pathologist are able to utilize histotechnologies to determine how diseased tissue differs from its physiological norm through this robust, yet delicate field. As a result, the field of pathology has become increasingly dependent on histotechnology and its subsequent applications. This is important for our work with the implantation of electrodes because fundamental knowledge of the electrode-tissue interface is critical for biocompatible designs and pathology of the surrounding tissue.

The present chapter discusses the steps to perform histology on peripheral nerve, a particularly dispiriting endeavor due to its soft tissue properties, and and how to qualitatively analyze the tissue post light microscopy to determine whether quantitative measures should be taken to further study morphology. A short dissertation on the effects of host-response of bioimplanted nerve tissues is provided, as the purpose of this report is to provide the groundwork for analyzing chronic implantation of electrodes.

3.2 History of Histology

The origins of histology, or the study of tissue structures via microscopy, could be traced back to the late 17th century when Marcello Malpighi visualized the pulmonary capillaries in a frog. Despite Malpighi's discovery, it wasn't entirely understood that various tissues were foundational to the structure of complex organ systems until the late 1700s when Marie Francois Xavier Bichat discovered their functionality. Bichat's discovery influenced the works of August Franz Josef Karl Mayer, a German anatomist and physiologist who coined the term histology in an 1819 publication. This led to the scientific study of histology establishment in 1826 when Thomas Hodgkin, most notably remembered for his discovery of Hodgkin's Lymphoma, collaborated with Joseph Jackson Lister to enlist a microscope to study the morphology of tissue properties. Together, they published a paper in 1827, "Notice of some microscopic observations of the blood and animal tissues," which has been revered as the foundation of modern histology. Lister's microscope work would lead to the design of the achromatic lens in the 1830s, greatly improving the resolution of microscopic imaging and increasing the span and availability of the field of histology.

As the scope of histology began to widen over the next century, tissue processing became increasingly more complex, expanding on discoveries made in the past and by experimenting with completely new techniques. It wasn't until the mid 1950s after the discovery of nerve conduction properties that histochemistry of the nervous system started to grow. Peripheral nerve tissue is particularly delicate due to its extracellular environment and mechanical properties. This makes it difficult to maintain the native structure prior to analysis post sectioning. Rosalind King published the Atlas of Peripheral Nerve Pathology which outlines current techniques for analysis of PNS tissue [58]. Our lab attempts to build on techniques outlined by King and the histotechnology community to fit our specific applications.

3.3 Processing, Embedding, and Staining

Tissue must be processed, embedded, and stained before its properties can be studied. This section focus' on these steps required to effectively preserve the nerve through processing, prepare the nerve for sectioning via embedding, sectioning, and staining for viewing. Each step plays a crucial role in ensuring the delicate tissue results in a viable segment for analysis. Proper technique is important, there is little room for error and failure to adhere to the histology processing standards may result in poor images, or even worse, loss of the specimen in its entirety. As such, a brief review as to the general goals of each component as well as potential issues that may result as failure to perform specific steps.

3.3.1 Fixation

The first step of tissue processing is fixation. Fixation involves preparing the tissue for the hydrophobic or hydrophilic embedding medium and prevents autolysis and putrefaction. Technologists, the individuals working to process tissue, must be well versed in the biological material under study and their intended form of embedding. For instance, biological material properties vary as a function of its cellular environment. Peripheral nerve is primarily soft tissue (Young's moduli of 576 ± 160 kPa in rat sciatic nerve), and is easily deformable [59]. Embedding media that shares a similar Young's modulus of the tissue may result in media dragging through the tissue upon sectioning. As a result, it is important to acknowledge the characteristics of the tissue when deciding upon a media for embedding, i.e., choosing between a hydrophilic or hydrophobic media. Hydrophobic media is typically utilized in soft-tissue processing. A hydrophobic media, methacrylate, is outlined in the present paper. In this case, the first step of processing is preservation of tissue in a solution of neutral buffer formalin (NBF) prior to submitting it to a series of dehydration steps, typically performed using ethanol. The dehydration steps are to remove water from the nerve that may interfere with the infiltration solution (added later). In some cases, we have noticed with the nerve tissue in our lab, it is required to further dehydrate the material using a sucrose solution to promote osmosis. Experience plays a critical role in this step, as it is possible to over-dehydrate the nerve, leading to a deformed micro-environment.

After dehydration has been completed, dehydrant must be removed to prevent unintended interaction with with the addition of infiltrating solution. Therefore the tissue should be soaked in a clearing agent, such as acetone, to remove all the added dehydrant. Once the dehydrant has been removed, the infiltration solution, which is typically the same material that is used to embed the nerve, is given time to mix with the tissue. Following infiltration, embedding of the nerve can take place.

3.3.2 Embedding

Embedding is rather simple compared to the aforementioned steps. In this step, the tissue is placed inside or affixed to the surface or mold that will hold the specimen in the orientation one wishes to perform sectioning (i.e., transverse, sagittal, etc.). The type of surface or mold used will depend on the sectioning one desires to perform (acrylic, cryogenic, paraffin, etc.). Furthermore, the technique used for embedding will vary depending on the embedding solution (determined during fixation). In our lab, we focused on using acrylic sectioning.

The primary steps involved in embedding in acrylic sectioning are placement of the specimen within the molding tray, followed by initiation of polymerization for hardening of embedding media, and lastly insertion of media into the tray. This leads to the media hardening in and around the nerve. Nerve becomes hard as a result of the prior infiltration step, where the hardening media was allowed to absorb into the specimen. After the nerve has become entirely solidified, it can be removed from the tray and prepared for sectioning.

3.3.3 Sectioning

Sectioning is very straight forward. The surface, or mold, is placed on a sample holder in a microtome. The microtome is the device used for sectioning tissue, which contains a knife, and can be set to a specific sectioning thickness. It is ideal to have a sharp knife that will not deform as a result of sectioning, however the knives go up in price depending on quality. In our lab, we used a Leitz 1512 Microtome with a 16 cm tungsten carbide knife (Delaware Diamond Knives, Inc.), which was suitable for cutting soft tissue and metal electrodes fixated in acrylic media.

3.3.4 Staining

The final step prior to visualization of tissue under light microscopy, staining, is optional; however, analysis of the cellular and extracellular environment of tissue is difficult without it. Staining is used to dye elements in the nerve, such as mitochondria, secretory granules, collagen, DNA, RNA, glycosaminoglycans, erythrocytes, etc. The mechanisms to which staining occur are relatively unknown aside from the fact that stains typically target either basic or acidic tissue elements. The method of staining varies from tissue to tissue, and may take time to perfect. It was our intent to create a protocol for the aforementioned steps in processing as well as modify a tissue staining regiment for use in analysis of peripheral nerve tissue studied in our lab.

There are many various dyes, however our lab utilizes two for peripheral nerve staining: Hematoxylin and Eosin (H&E) and Toluidine Blue (TB). H&E and TB are basic and acid dyes, respectively. As a result, these stains will interact with tissue of opposite nature; acid dyes interact with basic tissue elements, whereas the opposite is true for basic dyes. Basic elements include mitochondria, secretory granules, and collagen. Acidic elements include DNA, RNA, and glycosaminoglycans.

3.4 Structure of Peripheral Nerve

The peripheral nerve can be sectioned into three primary structures: epinuerium, pernieurium, and endoneurim. Each structural layer provides a crucial role to the overall health of the nerve. These roles include mechanical stability, diffusion control, and maintenance of a constant-pressure environment. Additionally, the morphology of the nerve will vary depending on the location a specimen has been extracted, such as proximal or distal to the central nervous system. A brief review of each structure as well as the characteristics of branching is provided to help improve the scope of using histology as a means to study the environment of peripheral nerve tissue. Fig. 3.1 provides an illustration of the morphology and anatomy of the peripheral nerve.

3.4.1 Epinueurium

The outermost covering of the peripheral nerve is composed of fibril-forming type I and type III collagen, a structure known as the epineurium [57]. A study by Seyer et al. indicated that the peripheral nerve was similar to human skin in its collagen content, containing 81% type I and 19% type III collagen with similar amino acid content of alpha1(I), alpha2, and alpha(III) chains [60]. Due to its large collagen extracellular content, the epineurium contributes to its tensile strength, however does not contribute to the barriers that protect its inner structures [61]. The epineurium is clearly visible using acidic dyes, which interact with the large collagenous environment.

3.4.2 Perineurium

Within the epineurium lies the perinuerium, a lamellar structure of large, flat perineurial cells immersed in tightly packed type III and type V collagen. This layered arrangement of collage is directly proportional to the number and size of the fascicle and is primary diffusion barrier for the nerve [61]. One important characteristic of perineurium structural proteins is its heparin sulfate content, providing a negative charge and functions as an extracellular molecular filter. The negatively charged heparain sulfate can be identified using an acidic dye, and appears as an easily contrastable sheath between the adjacent epineurium and endoneurium.

3.4.3 Endoneurium

Endoneurial tissue is the innermost of the three connective layers, and lies in closest proximity to the nerve axon and, in the case of myelinated axons, the myelin sheath. The endoneurium contains blood vessels that create a blood-nerve barrier, analogous to the brains, via tight junctions that separate the endoneurium from circulating blood [61]. The extracellular environment is similar to the epineurium, containing collagen type I and III, however it is more densely packed than the prior. The endoneurium plays a critical role in fluid pressure, maintaining a light positive pressure that guarantees a constant environment [62]. Additionally, the endoneurium contains Schwann cells, which are responsible for mylination of the adjacent nerve fibers for saltatory conduction. Schwann cells may be identified using a basic dye when staining.

3.4.4 Nerve Fascicle Compartmentalization

As nerves project outward from the central nervous system to the far reaches of the PNS, they repeatedly divide and unite to form plexus', leading to various changes in morphology of nerve cross-sectional area (see Fig. 3.1 [63, 64]). This can be viewed as compartmentalization of the nerve fascicles to form a large, uni-fascicular segment that may later divide into multiple fascicles prior to separating for innervation of various receptor locations at the distal end of the peripheral nerve, a process referred to as cross-branching [64]. In these cross-branched environments, many endoneurial tracts come together to form fascicles surrounded by perineurium sheaths. These sheaths are then entrapped in an epineurial layer that sit adjacent to another fascicle surrounded by perinuerium. The greatest degree of uniform fascicular arrangement occur in the major nerves of extremities [64]. Fig. 3.1 is an illustration of the cross- and longitudinal sections of the peripheral nerve.

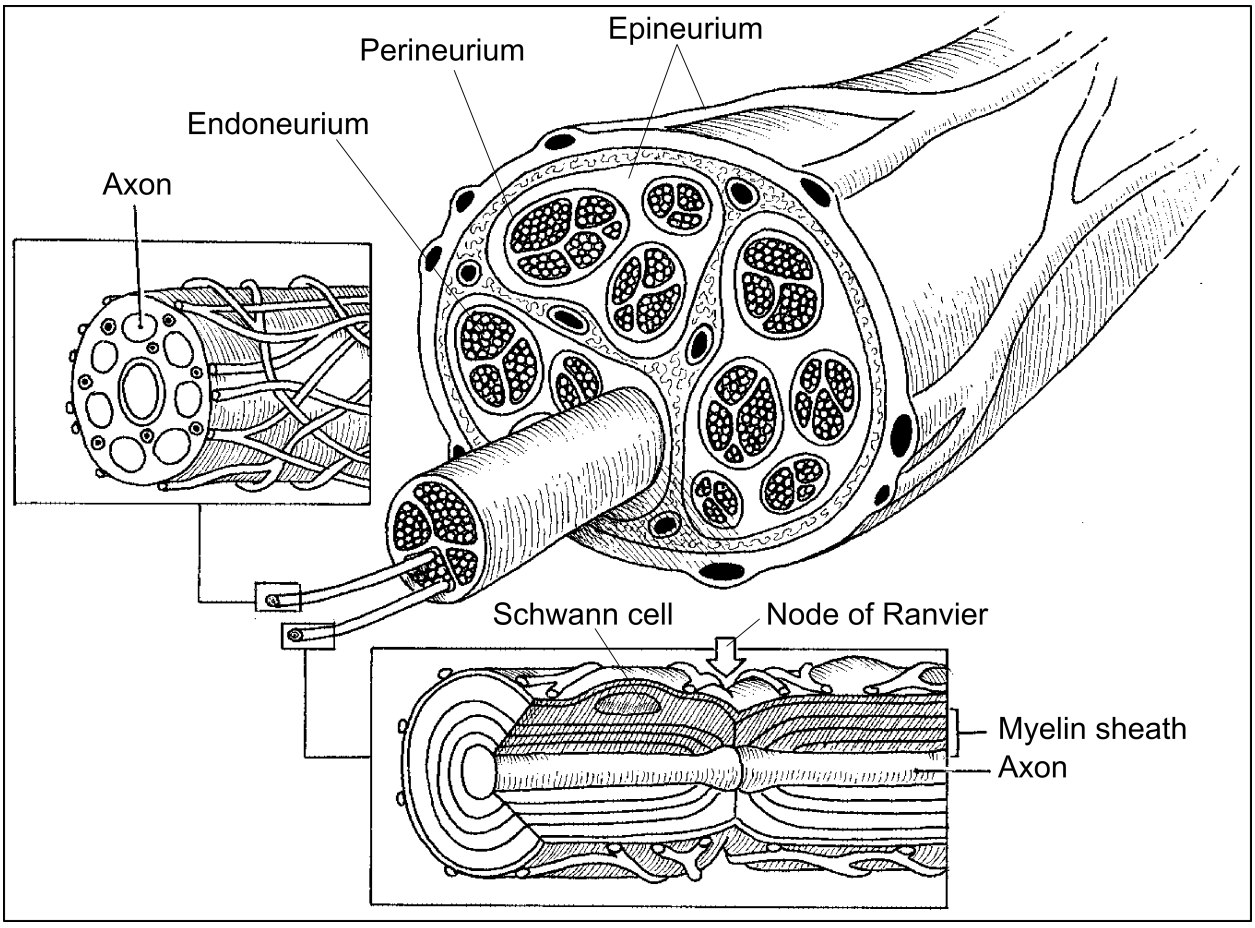

Figure 3.1. Peripheral nerve anatomy. Adapted from "Nerve Injury and Repair" with permission [55].

3.5 Biological Response to Implanted Electrodes

Any material that comes into contact with a biological system will have some sort of impact on the cellular environment. In biomedical intervention, the goal is to minimize this impact as much as possible irrespective of the form of therapy. Our lab's current goal is to design biomedical electrochemical interfaces that will be used in our chronic studies to explore the outcomes of low-frequency alternating current as well as the effects of implantation of various electrode designs on living mammalian tissue. Henceforth, it is necessary to have a means of analyzing the tissue throughout the duration of a study.

The inflammatory, bio-incompatible, and biocompatible response to subcutaneously placed electrodes was studied by Grill and Mortimer. It was determined that the inflammatory response is outlined by tissue encapsulation. In the case of bio-incompatible electrodes, the inflammatory response was intensified, leading to an innate immune response with a significant number of macrophages, increased collagen content and foreign body giant cells. However, this contrasted greatly to the biocompatible response in which the inflammatory response subsided, resulting in an increase of lightly packed fibroblasts, collagen, and macrophages around the electrode.

The study by Grill and Mortimer is extremely relevant to the future aims of our lab. They introduced the effects that an immune response has on the impedance of electrodes, which is important for chronic studies. With the development of a new PEDOT:PSS/CB solution, it will be necessary to identify any synthetic material that may become displaced as a result of implantation or continuous stimulation. This may further invoke an inflammatory response, leading to a potential immune response resulting in disruptive change to the surrounding environment.

3.6 Methods

Various processing and sectioning methods were explored to widen our labs histology capabilities. Many of the methods described below required numerous trial and error before optimal processing, sectioning, and staining could be achieved. The most difficult matter will always remains that every tissue that comes from an organism is uniquely complex in that no organism shares the same biochemical properties. Consequently, the succeeding methods are merely based on an absolute mean of the peripheral nerve tissue handled in our lab, meaning that the methods may vary from tissue to tissue, and the more experience a technologist has will lead to improve stained tissue quality.

3.6.1 Paraffin, Acrylic, and Cryogenic Processing and Sectioning Protocols

3.6.1.1 Paraffin

Paraffin embedded specimens were routinely processed in accordance to Carson et al., from Histotechnology 4e, protocol 2 [65]. Serial sectioning was performed using a HistoCore MULTICUT (Leica Biosystems).

3.6.1.2 Acrylic

Acrylic processing was performed using the Technovit Glycol Methacrylate Kit 8100 (Electron Microscopy Sciences). Prior to embedding, nerve tissue was fixed in 10% neutral buffer formalin (Fisher Scientific, CAS 50-00-0) for more than 24 hours. Following fixation, the tissue was placed in a phosphate buffer saline (PBS) (Fisher Scientific, CAS 7731-18-5) at pH 7.4 with 6.8% (w/w) sucrose for 12 hours. Dehydration was performed using three acetone (Fisher Scientific, CAS 67-64-1) baths whereby tissue was bathed for 20 minutes each. Upon completion of the acetone bath, tissue was blotted dry using Kimwipes (Kimberly-Clark, 34155) and placed in a 15 mL conical vile (Fisher Scientific, 339650) prepared with the infiltration solution (Electron Microscopy Sciences, 14654) and stored for 12 to 24 hours. After the required time elapsed, the nerve was separated into 5 mm segments to prepare for embedding. The embedding solution (Electron Microscopy Sciences, 14654) was deposited into wells of a molding tray such to prevent formation of bubbles, whereby the nerve was immediately positioned appropriately inside the well. Once all the sectioned nerves were properly positioned, the wells were covered with a plastic film, and the tray was placed in a refrigerator (2 $^{\circ}C$) for three hours to facilitate the polymerization of the embedding medium. Polymerized media was removed from the refrigerator, the plastic film was removed, and Histobloc's (Electron Microscopy Sciences, 14654-60) were placed on the surface of the molds. Histobloc's were attached using the Technovit 3040 Mounting Medium (Electron Microscopy Sciences, 14652) and allowed to harden for 15 minutes prior to removing the glycol methacrylate molds containing the nerve tissue from the wells. Sectioning was performed using a Leitz 1512 Microtome with a tungsten carbide knife (Delaware Diamond Knives, Inc.) and samples were sectioned between 1 and 20 μm.

A charged microscope slide was placed on a hot plate. Using a squeeze/ wash bottle, a layer of $_{dd}H_2O$ was placed on the microscope slide. Immediately after sectioning the nerve, fine forceps were used to place the nerve in the layer of water on the charged microscope slide, where it was oriented to the intended position; excess water was then discarded. The slide was then moved to the outer rim of the hot plate (preventing it from getting too hot) and allowed to dry for five minutes. After the slide was dried, it was removed for staining.

3.6.1.3 Cryogenic

A cubicle biopsy Cryomold (Electron Microscopy Sciences, 62534-10) was filled with O.C.T. Compound (Fisher Scientific, 23-730-572). Nerve tissue was sectioned into approximately 5 mm sections before being carefully situated within the Cryomold to prevent formation of bubbles. The O.C.T. Compound was flash-frozen using liquid nitrogen and the solid structure was removed from the Cryomold and affixed to a cryostat embedding chuck (Electron Microscopy Sciences, 70171-03) primed with a layer O.C.T. Compound. The chuck was immediate placed within a Cryostat (Leica 2800E Frigocut Microtome Cryostat) with a box and object temperature of -26 $^{\circ}C$ and -21 $^{\circ}C$, respectively. Additional O.C.T. Compound was progressively placed around the solid cubicle structure after it was affixed to the chuck to ensure it would remain stationary during the sectioning process. After properly fixing the tissue to the chuck, it was allowed to equilibrate with the ambient temperature of the cryostat for at least 5 minutes prior to sectioning. Sectioning was performed using a Histo Knife (Electron Microscopy Sciences, 14653-13), and sections were cut between three and 20 μm. Sectioned tissue was placed on a polarized microscope slide and submersed in a 90% EtOH solution for 15 seconds immediately following sectioning.

3.6.2 Staining Protocols

3.6.2.1 Hematoxylin and Eosin Staining Protocols

H&E staining protocols were developed based on the three methods discussed for tissue processing: acrylic, paraffin, or cryogenic (cryo). Protocols vary as a function of numerous variables associated with pre-processing of the nerve. For instance, a flash-frozen nerve for use in cryo-sectioning is encased in OCT compound, an amphipathic substance that will prevent the stain from penetrating the nerve. Removal of this compound, using water, is necessary prior to initiating the staining protocol. Another example, paraffin processing, requires a xylene or a xylene substitute to remove the paraffin seal. It is important to keep in mind that the processing and embedding is performed to preserve the nerve and keep the nerve structure intact prior to sectioning. Once sectioned, the embedding media should be removed to prevent it from interfering with the stain. Furthermore, it should be noted that the clearing process described in each protocol is dependent on the embedding media used, and therefore each staining protocol is described henceforth as a function of the embedding media. Once the media has been effectively removed, each protocol follows generally the same trend. Removal of the media is performed immediately prior to staining and is described below.

H&E staining can be performed in one of two possible protocols: progressive or regressive. In the regressive staining protocol, the tissue is overstained, and excess dye is then cleared using an acid rinse (typically acetic or hydrochloric acid) until an optimum intensity is achieved. This requires precision and a good grasp on how quickly the stain may be removed by the acid rinse which is typically achieved through experience with regressive staining because the amount of stain in a tissue varies as a function of the type of tissue and thickness of the section. For progressive staining, an attempt to obtain the optimal characteristics is made without the use of an acid (which would be used in a regressive staining protocol). This method of staining is preferred if staining is consistent across a large sample of similar tissue.

3.6.2.1.1. Paraffin (Progressive Staining Protocol)

Paraffin sectioned PNS tissue that has been affixed to a slide was placed in a xylene (Fisher Chemical, CAS 7758-09-0) bath and allowed to soak for three minutes, and subsequently moved to two additional baths in a contiguous manner upon completion of the three minutes, consequentially removing the paraffin substrate. The slide was then placed in three 100% reagent alcohol (Fisher Chemical, CAS 64-17-5), composed of 90% ethanol (EtOH), solutions for one minute each. Slides were introduced to a reagent alcohol solution diluted to a 95% (v/v) mixture with deionized water ($_{dd}H_2O$) and allowed to soak in two baths for one minute each; finally slides were placed in an additional bath containing 70% (v/v) EtOH, re-hydrating the tissue. Upon completion of the re-hydration via decreasing EtOH concentrations, the tissue was prepared for hematoxylin staining using three ($_{dd}H_2O$) baths whereby slides were allowed to bathe for one minute each. The progressive hematoxylin staining was performed by submitting the tissue to a Mayer's hematoxylin bath for three minutes. The tissue was kept hydrated by using three subsequent $_{dd}H_2O$ baths, where the tissue was allowed to rest for two minutes each. A 1% (w/w) sodium bicarbonate ($NaHCO_3$) solution was used as the bluing agent and was required to interact with the tissue for one minute. The tissue was then viewed under a microscope to confirm it obtained adequate staining of acidophilic regions, which was confirmed by adequate exposure of Schwann cells. Excess $NaHCO_3$ was then rinsed during three subsequent water baths, allowing the tissue to soak for two minutes each. Eosin was used as the counter-stain, and tissue was submersed for roughly one minute and excess eosin was removed using a method similar to the reverse-order of the alcohol baths previously mentioned for hydration (70% EtOH followed by a single 95% EtOH and two 100% EtOH baths for one minute each). After dehydration, tissue was submerged into a pure xylene bath for three minutes before being allowed to dry prior to placement of the cover-slide. Table 3.1 provides the steps fo the aforementioned protocol.

3.6.2.1.2. Acrylic (Progressive Staining Protocol)

Acrylic sectioned PNS tissue was immediately placed in Gill's II Hematoxylin (Sigma-Aldrich, GHS216-500ML) for three minutes following affixing to a slide. Tissue was kept hydrated using tap water (pH. 7.70), which also acted as the bluing agent. A total of three tap water baths were used, with the tissue resting in the first two for two minutes each followed by submersion for two minutes and five consecutive dunks in the last water bath. Eosin B (Sigma-Aldrich, 56360-46-3) was introduced as the counter-stain, and the tissue was submerged for three minutes. $_{dd}H_2O$ was then used to remove any excess eosin in two baths, where the tissue was soaked for two minutes in the first bath followed by 10 dips in the second. Two xylene baths were then used to remove any impurities and to dry out the tissue prior to placing the cover-slide, where the tissue was allowed to rest for three minutes in the first bath followed by 10 dips in the second. A coverslip was then placed on the slide to prevent the surface from becoming contaminated. Table 3.2 provides the steps for the aforementioned protocol.

3.6.2.1.3. Cryogenic (Regressive Staining Protocol)

Frozen sectioned PNS tissue that has been affixed to a slide is dipped consecutively in three ${}_{dd}H_2O$ baths for three dips each or until the OCT compound has been removed. Upon removal, the tissue was introduced to Gill's II Hematoxylin for three minutes. Tissue was kept hydrated by consecutively dipping the slide into three ${}_{dd}H_2O$ baths for five dips each before being placed into a 0.5% (v/v) acetic acid alcohol solution to remove excess hematoxylin. Tissue was submerged in ${}_{dd}H_2O$ for five dunks each in three baths to remove the acid alcohol solution prior to bluing, which occurred by dipping the tissue 10 times consecutively in a 1% (w/w) $NaHCO_3$ in ${}_{dd}H_2O$ solution. Excess bluing agent was washed away using three ${}_{dd}H_2O$ baths, where slides were dipped five time each before being moved to the next bath. Tissue was placed in an eosin bath for 10 dips and allowed to bathe for one minute to counter-stain. Excess eosin was removed using a 95% (v/v) reagent alcohol solution for 10 dips in two baths each before being moved to a 100% reagent alcohol solution for an additional 10 dips. The slide was then submitted to a xylene bath (two minutes) to remove any impurities and assist in the drying of the tissue prior to cover-sliding. Table 3.3 below provides the aforementioned steps.

3.6.2.2 Toluidine Blue Protocols

3.6.2.2.1. Acrylic and Cryogenic TB Protocol

Toluidine blue staining solution was prepared in accordance with Seifert, P. by mixing 1 g toludine blue O (Sigma-Aldrich, CAS 92-31-9) with 1 g of sodium tetraborate decahydrate (Sigma-Aldrich, CAS 1303-96-4) in 98 mL of distilled water to produce a total of 100 mL of 1% toluidine blue [66]. Slides that contained affixed acrylic embedded tissue were placed on a slide warmer with a set-point of 50 $^{\circ}C$ and allowed to dry for 30 seconds to ensure temperature equilibrium with the surface prior to staining. A single drop of filtered 1% toluidine blue was then deposited on-top of the dried tissue and allowed to soak for 15 seconds before being placed in a coplin jar filled with ${}_{dd}H_2O$ to prevent over-staining. The tissue was allowed to rest for 60 seconds before being moved to two additional ${}_{dd}H_2O$ filled coplin jars, where they bathed for an additional 60 seconds each. Excess water was absorbed using a Kimwipe (Kimberly-Clark) and the slide was dried on the slide warmer for 5 minutes at 40 $^{\circ}C$ or until it exhibited no signs of moisture. Finally, the slide was submerged in a xylene bath to remove any remaining impurities before placement of the glass cover slip. Table 3.4 below provides the steps for the TB staining protocol.

3.6.3 Light Microscopy to Analyze Stains

At various points throughout the sectioning process, light microscopy was used to analyze whether the tissue was successfully sectioned and intensity of the stain; this occurred prior to staining to ensure adequate sectioning, after acid rinse during H&E regressive protocol, after bluing in H&E staining, and immediately following TB staining, Key qualitative components for correct detection of tissue properties were addressed to ensure appropriate staining techniques, allowing for a quantitative characterization via an image processing program, such as ImageJ. In the absence of staining, one of the foremost indicators for an incorrect section includes the presence of streaking across the longitudinal axis of the nerve, considering the goal was to achieve a transverse orientation, indicated by a graded section or cutting across the vertical axis of the axon. Additional indications of poor sectioning include visible Nodes of Ranvier in myelinated fibers (arising from a longitudinal section), separation between adjacent layers of nerve, such as the detachment of the epineurium from the perineurium or perineurium from the endoneurium, tearing of the nerve which can be identified by a rift formed within a layer of the connective tissue, and overlapping or folding of the adjacent layers.

Once the tissues have been stained, properties of the stain will bring out various components of the studied tissue. H&E staining leads to identification of the nuclei (dark blue), red blood cells and eosinophil granules (red), cytoplasm and myelin (pink), and collagen (light pink) of the nerve [49]. In contrast, toluidine blue should provide dark-purple nuclei, purple erythrocytes, lavender cytoplasm, and gray-blue fats and lipids [67].

3.7 Results

Nerves were processed, and embedded using paraffin, acrylic, and cryogenic processing techniques. Tissues were then sectioned and stained using one of two potential methods: Hematoxylin and Eosin (H&E) or Toluidine Blue (TB). The results are depicted in Fig. 3.2 below.

Fig. 3.2a and Fig. 3.2d illustrate that the TB method was effective in viewing basic molecular structures, such as the myelin sheath which is composed of a basic molecule, sphingomyelin. H&E effectively contrasted the three neural tissue layers: epineurium, perineurium, and endoneurium. This can be seen in Fig. 3.2b and Fig. 3.2c, which clearly show the acidic biomolecular structures found in nerve tissue. These structures include nuclei from Schwann cells in the endoneurium, erythrocytes innervating the nerve throughout the endoneurium and adjacent to the nerve in capillaries, and hyaluronic acid located in the extracellular matrix of the perineurium. In both TB and H&E scenarios, collagen is stained and contrasts as a function of its density within each structure.

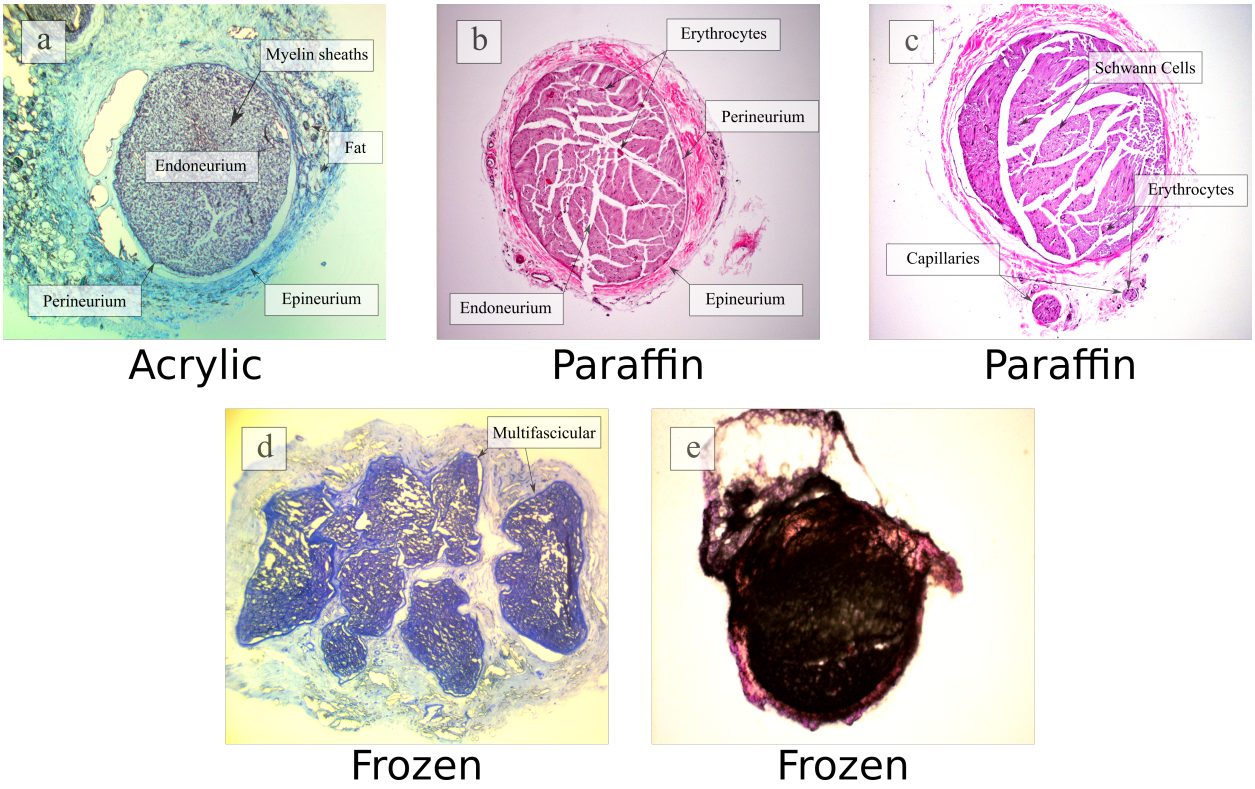

Figure 3.2. Stained nerve tissue. Blue dyes are Toluidine Blue (TB), purple-pink dyes are Hematoxylin and Eosin (H&E). (a) TB stain of canine vagus nerve, contrasts the various layers of the nerve: epineurium (loose collagen matrix), perineurium (lamellar structure), and endoneurium. Within the endoneurium lies a plethora of myelinated fibers, which can be identified by the concentric blue stains. Fat can be seen residing on the exterior of the epineurium, noted by its globular structure. (b) H&E stain of rat sciatic nerve, visible contrasting between the three layers of the nerve. H&E allows for identification of erythrocytes that innervate the endoneurium of the nerve. (c) H&E stain of rat sciatic nerve, capillaries can be seen residing outside the epineurium. Within the enodneurium Schwann cells are dispersed adjacent to fibers. (d) TB stain of swine phrenic nerve, shows a multifascicular nerve structure. The specimen was sectioned on a slight gradient, failing to cut transversely results in identification of the longitudinal myelinated axon sheath, bearing a resemblance to sausage links. (e) H&E stain or rat sciatic nerve, over-staining and poor sectioning resulted in a nerve that is no longer viable for viewing or quantitative and qualitative analysis.

Poor staining can result in what is shown in Fig. 3.2e, where the nerve has become blackened from excessive hematoxylin and blueing agent. In addition to its poor stain, it shows signs of tearing as a result of over-dehydration of the nerve during processing and folding in result to incorrectly positioning the nerve on the microscope slide, or loss of adhesion during the staining process. Similar breaking can be seen in Fig. 3.2b and Fig. 3.2c, however the neural matrix has remained fairly well intact despite the structural deformities. Fig. 3.3 shows two nerves that are awaiting to be stained. Fig. 3.3a indicates small signs of spearation of the perineurium from the epineurium as well as some dragging (smearing) resulting from the a potentially loose microtome blade. Fig. 3.3b shows the epineurium has pulled back from the surface of the nerve in the southeastern corner of the fascicle, the perineurium has remained intact.

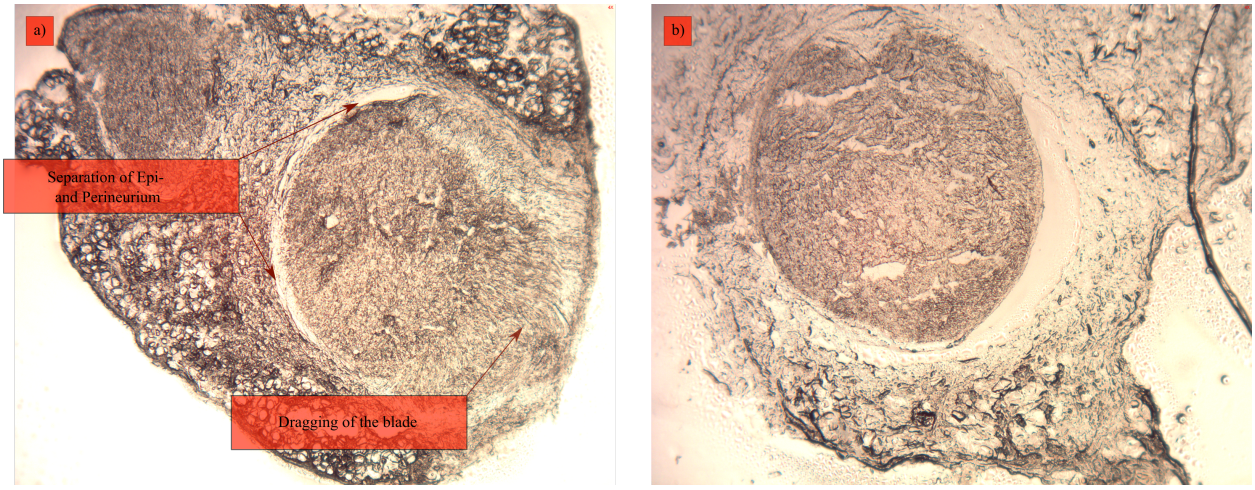

Figure 3.3. Unstained canine vagus nerve. (a) Separation between the epineurial and perineurial layers; smearing indicates there has been dragging of the blade. (b) Partial retraction of the perineurium from the epineurium in the southeastern region of the fascicle.

Figure 3.4 shows a poorly sectioned nerve that would not be viable for staining. The folding of the nerve (see figure) would result in over-staining of the folded region. Staining in this region would appear to be similar to Fig. 3.2e where the nerve is dark. Fat intermixing with the epineurium is common for nerves that have been poorly sectioned as a result to microtome dragging, and can be visible adjacent to the dragging section where the fat is bleeding into the nerve in the same direction.

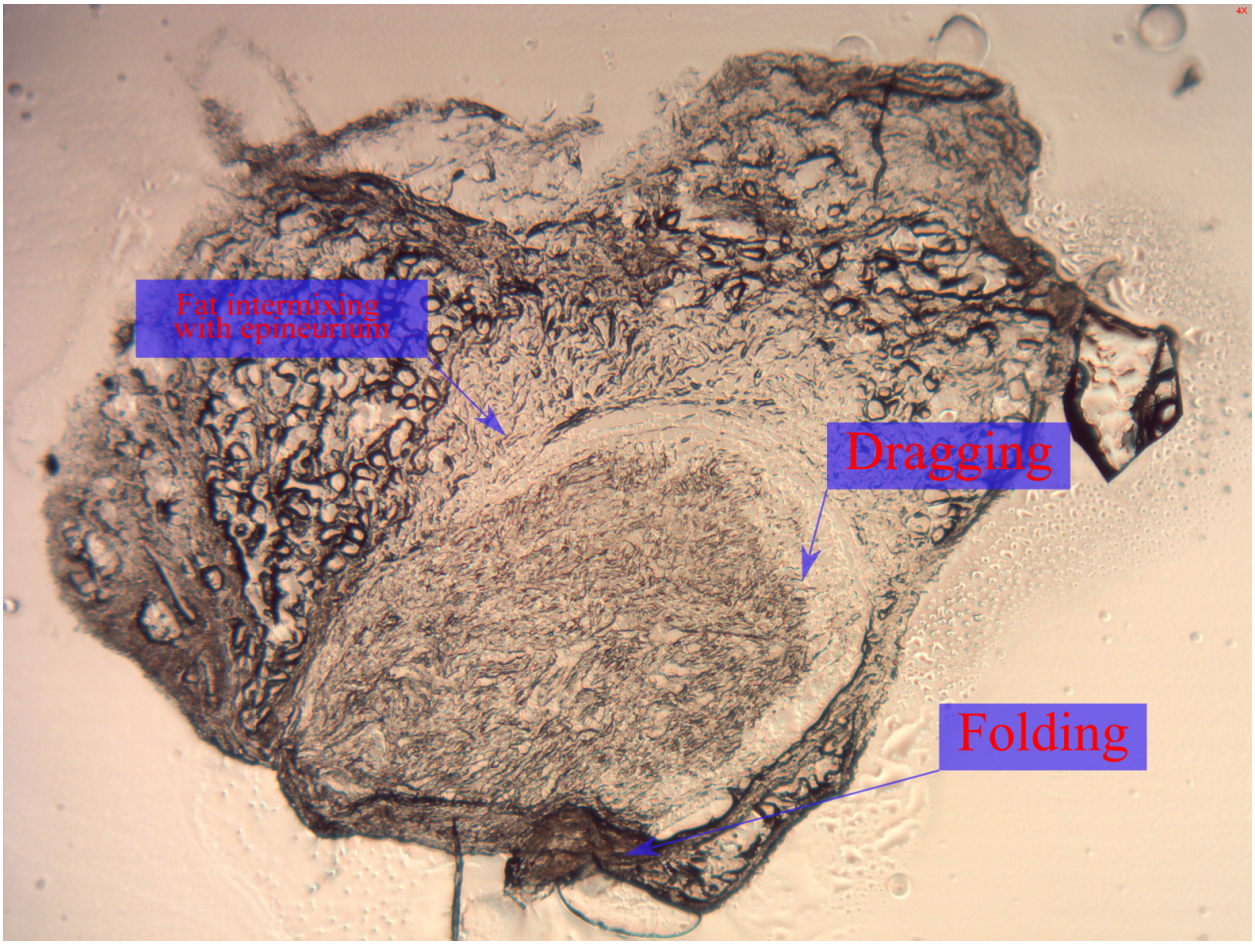

Figure 3.4. Canine vagus nerve that has been poorly sectioned; poor sectioning led to bleeding of fat into the region where the epineurium is located. A folded region is identified in the southernmost portion of the fascicle.

3.7.1 Hematoxylin and Eosin

H&E is a basic dye, and therefore stains acid tissue elements. Acidic tissue elements that are found in the peripheral nerve include hyluronic acid, nuclei of Schwann cells, fibroblasts, and acidc glycoproteins. Fig. 3.5 is an example of what a common H&E section at various magnifications looks like. The depiction is a swine vagus nerve that was cut 6 μm thick via a cryostat. Fig. 3.5a is a 4x magnification of the nerve, showing the complete diameter (approximately 2.80 mm) of the nerve and its residing tissue elements. The vacant spaces located in the center and towards the periphery of the transverse section once contained fat (not captioned) and some surrounded adipocytes intertwined with epineurial collagen. This is typically washed away during the staining process, giving rise to the vacancy, however, some adipocyte nuclei may be identified lining this space. As previously described, the epinuerium is composed of loose collagen fibrils that appear as a light pink stain and contain vessels that supply nutrients to the epineurial cells (Fig. 3.5b). In the perineurium, the collagen layers begin to darken to a light purple as a result of the hyaluronic acid, increased density, and fibroblast nuclei that line the circular, lamellar structure. The endoneurium (Fig. 3.5c) is seen within a fascicle of approximately 250 μm in diameter, and contains numerous Schwann cells, which are stained dark purple. The lamellar structure of the perineurium is not as easily identifiable as seen in Fig. 3.2b, however, in Fig. 3.5b the perineurial lamellae can be made visible by locating the fibroblast cells that radially align the endoneurium-perineurium boundary.

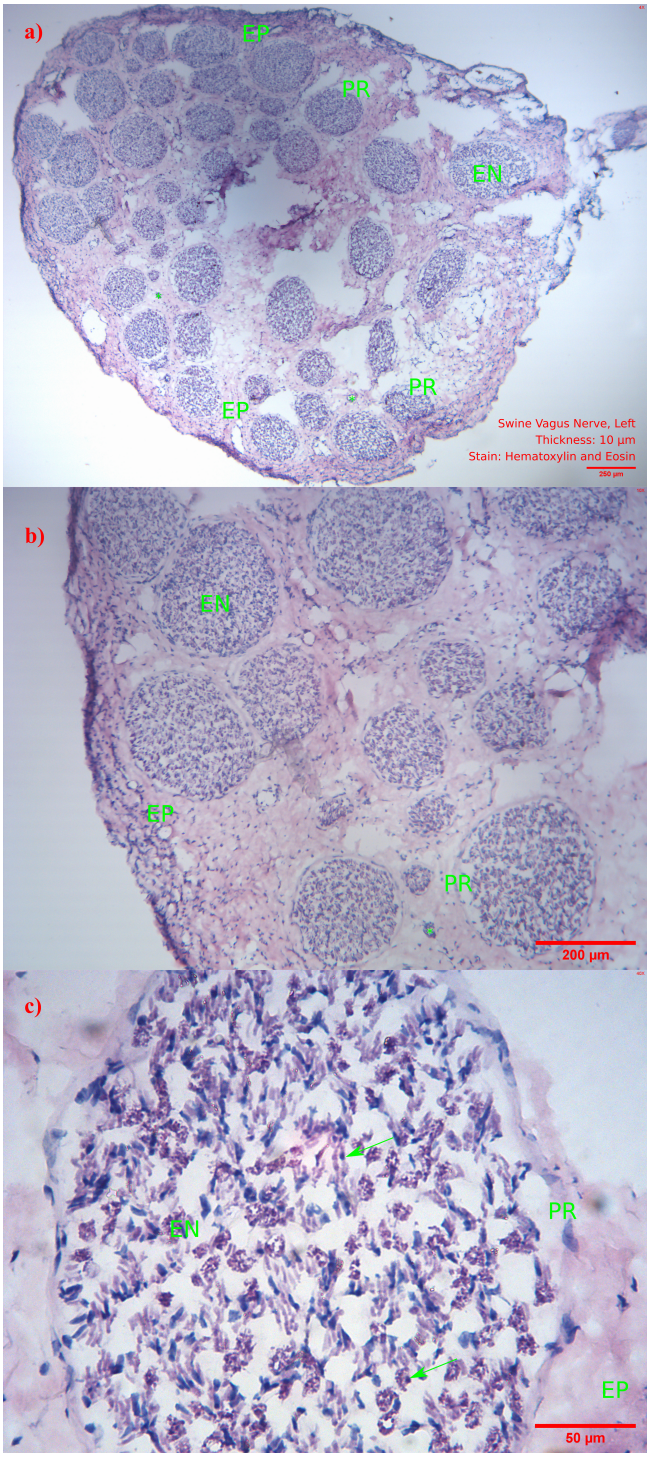

Figure 3.5. Cryogenic section of a multifascicular swine vagus nerve stained by H&E, sectioned 6 μm thick. EP = Epineurium; PR = Perineurium; EN = Endoneurium; arrow, nucleus of Schwann; *, vessel. (a) 4X magnification; cross-section of the entire nerve, approximately 2.80 mm in diameter. (b) 10X magnification. (c) 40X magnification; endoneurium, fascicle approximately 250 μm in diameter.

3.7.2 Toluidine Blue Stain

TB is an acidic dye and therefore stains basic tissue elements. Basic tissue elements that are found in the peripheral nerve include collagen, basic glycoproteins, mast cells, and myelin. TB is typically used to contrast the various densities of collagen and to identify the myelin sheaths in myelinated axons. Fig. 3.6 is an example of TB stained tissue at various magnifications. The illustration is two 3 μm acrylic sections of a swine vagus nerve excised on the same date as the image shown in Fig. 3.6. The left and right side of the figure represent the left and right vagus nerve, respectively. Fig. 3.6a and 3.6d are a 4X magnification of the vagus nerve, approximately 2.80 mm and 2.60 mm in diameter, respectively. Across the transverse section of the nerve, collagen can be identified. The epineurium appears as a dispersed boundary of collagen fibrils that bare no direction, however in Fig. 3.6b and Fig. 3.6d the perinuerial collagen can be seen as a dense lamellar structure relative to the epineurium; also visible are vessels which supply nutrients to the surrounding structures. Fig. 3.6c and Fig. 3.6e show the endoneurium of one of the fascicles (approximately 334 μm and 250 μm, respectively) as well as its underlying structures: mast cells, collagen, and meylinated fibers.

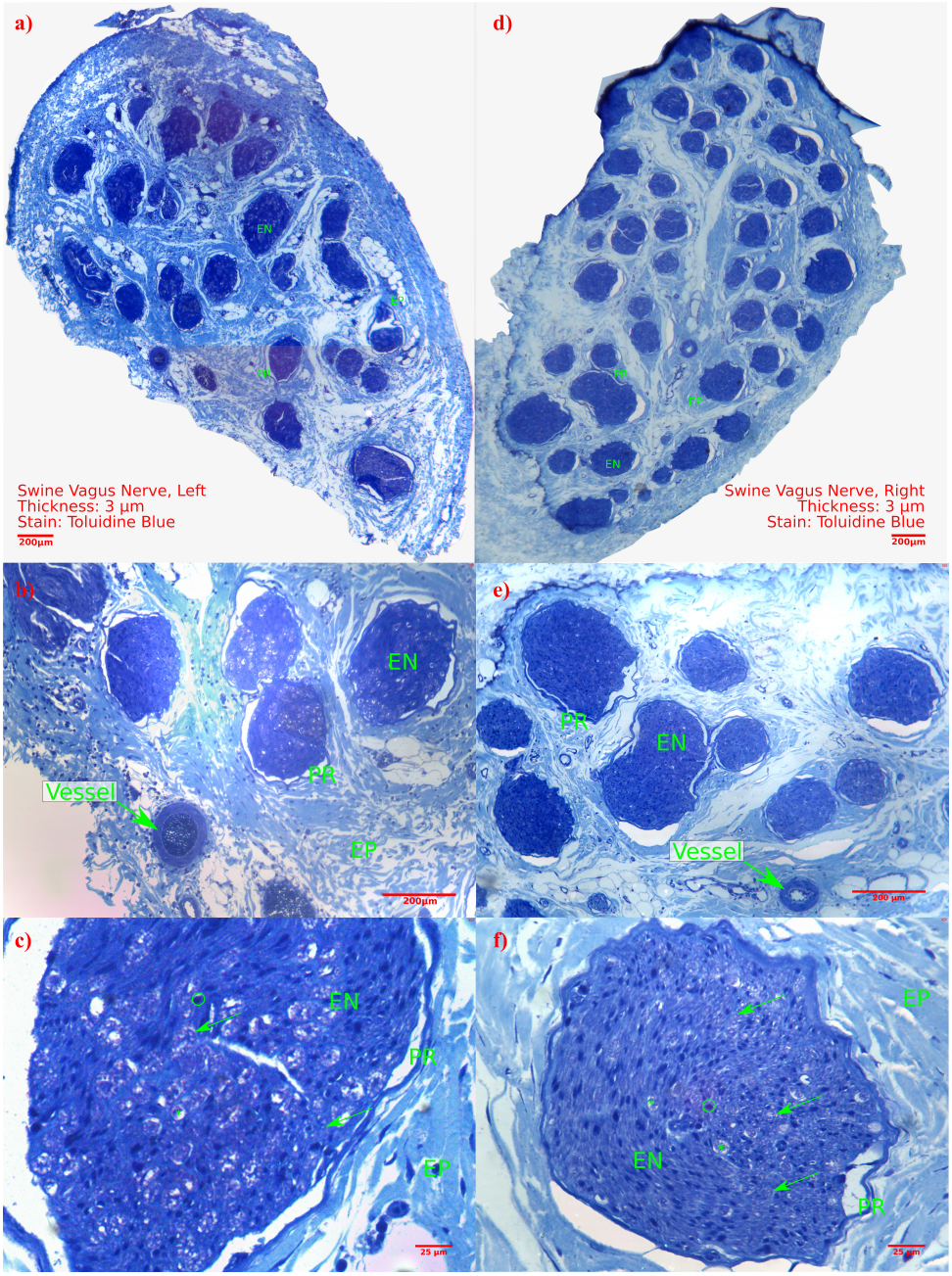

Figure 3.6. Acrylic sections of a swine vagus nerve. EN = Endoneurium; PR = Perineurium; arrow, myelin; circle, mast cell; EP = Epineurium; 20a – 20c are of a left vagal nerve, 20d – 20e are of the right vagal nerve. (a) 4X magnification of the left vagus nerve, approximately 2.80 mm in diameter. (b) 10X magnification. (c) 40X magnification, fascicle of approximately 334 μm in diameter. (d) 4X magnification of the right vagus nerve, approximately 2.60 mm in diameter. (e) 10X maginification. (f) 40X magnification, fascicle of approximately 250 μm in diameter.

Table 3.1. Paraffin Progressive Staining Protocol.

Step	Chemical	Resonance Time	Notes
1	Xylene	3 min.	
2	Xylene	3 min.	
3	Xylene	3 min.	
4	100% EtOH	1 min.	
5	100% EtOH	1 min.	
6	100% EtOH	1 min.	
7	95% EtOH	1 min.	
8	95% EtOH	1 min.	
9	70 % EtOH	1 min.	
10	$_{dd}H_2O$	1 min.	
11	$_{dd}H_2O$	1 min.	
12	$_{dd}H_2O$	1 min.	
13	Hematoxylin	3 min.	
14	$_{dd}H_2O$	2 min.	Replace water if deep purple
15	$_{dd}H_2O$	2 min.	Replace water if light purple
16	$_{dd}H_2O$	2 min.	Replace water if any purple
17	$NaHCO_3$ (Sodium Bicarbonate)	1 min.	Verify stain by viewing slide under microscope
18	$_{dd}H_2O$	2 min.	Replace water if blue
19	$_{dd}H_2O$	2 min.	Replace water if blue
20	$_{dd}H_2O$	2 min.	Replace water if blue
21	Eosin	1 min.	
22	70% EtOH	1 min.	
23	95% EtOH	1 min.	
24	100% EtOH	1 min.	
25	100% EtOH	1 min.	
26	Xylene	3 min.	
27	Xylene	3 min.	
28	Xylene	3 min.	
29	Coverslip		Use Acrytol Mounting Medium

Table 3.2. Acrylic H&E Progressive Staining Protocol.

Step	Chemical	Resonance Time	Notes
1	Gill's II Hematoxylin	4 min.	
2	Tap Water (alkaline)	2 min.	
3	Tap Water (alkaline)	2 min.	
4	Tap Water (alkaline)	5 dips + 2 min.	
5	Eosin	3 min.	
6	Tap Water	2 min.	
7	Tap Water	10 dips	
8	Xylene	3 min.	
9	Xylene	5 dips	
10	Xylene	5 dips	
11	Coverslip		Use Acrytol Mounting Medium

Table 3.3. Cryogenic H&E Regressive Staining Protocol.

Step	Chemical	Resonance Time	Notes
1	$_{dd}H_2O$	3 dips	
2	$_{dd}H_2O$	3 dips	
3	$_{dd}H_2O$	3 dips	
4	Gill's II Hematoxylin	3 min.	
5	$_{dd}H_2O$	5 dips	Replace water if deep purple
6	$_{dd}H_2O$	5 dips	Replace water if light purple
7	$_{dd}H_2O$	5 dips	Replace water if any purple
8	0.5% Acetic Acid Solution	1 dip	
9	$_{dd}H_2O$	5 dips	
10	$_{dd}H_2O$	5 dips	
11	$_{dd}H_2O$	5 dips	
12	$NaHCO_3$ (Sodium Bicarbonate)	10 dips	
13	$_{dd}H_2O$	5 dips	
14	$_{dd}H_2O$	5 dips	
15	$_{dd}H_2O$	5 dips	
16	95% EtOH	5 dips	
17	Eosin	10 dips + 1 min. soak	
18	95% EtOH	10 dips	Replace if dark pink
19	95% EtOH	10 dips	Replace if light pink
20	100% EtOH	10 dips	Replace if any pink
21	100% EtOH	10 dips	Replace if any pink
22	Xylene	2 min. soak	Replace if pink
23	Xylene	10 dips	
24	Coverslip		Use Acrytol Mounting Medium

Table 3.4. Acrylic and Cryogenic TB Protocols.

Step	Chemical	Resonance Time	Notes
1	Toluidine Blue	1 drop + 15 second soak	Must be performed on a slide warmer at 50 ^{circ}C
2	$_{dd}H_2O$	60 seconds	
3	$_{dd}H_2O$	60 seconds	
4	$_{dd}H_2O$	60 seconds	
5	Kimwipe		Remove excess water residing on slide
6	slidewarmer	5 minutes	40 $^{\circ}C$ until no signs of moisture
7	Xylene	2 minutes	Replace if any blue
8	Xylene	10 dips	
9	Coverslip		Use Acrytol Mounting Medium

CHAPTER 4. DISCUSSION

The present study had two aims: (1) Explore PEDOT:PSS/CB as a potential new interface as opposed to PEDOT:PSS; (2) Design a histology protocol to analyze peripheral nerve tissue following implantation of conventional electrodes modified with PEDOT:PSS/CB. In the current chapter I review the results obtained from each aim, relevant technical issues, possible improvements, and future steps. One new application that will be introduced in this chapter is low-frequency alternating current (LFAC) and how the modified PEDOT:PSS with CB will potentially contribute to its success.

4.1 Exploration of PEDOT:PSS/CB

PEDOT:PSS is not a new method for reducing the impedance of the electrochemical interface in electrodes for neuromodulation. Various electrode manufacturing companies and researchers have studied many methods of creating a suitable and stable structure. Previously successful techniques include sputtering and chemical oxidation [21, 34, 43]. However, sputtering is expensive and chemical oxidation can be quite difficult to achieve if you do not have a suitable space or setup for using potentially hazardous chemicals. Electrodeposition has been employed by others and has been the go-to method for reducing interfacial impedance in electrodes in our lab because of its cheap and reproducible results. Unfortunately, we have discovered that the deposited substrate is easily removed when sheared; this applies to relatively soft environments such as those found in mammalian tissue. The primary goal of exploring PEDOT:PSS/CB was to determine if the newly synthesized substrate would have a mechanical advantage to its PEDOT:PSS-only counterpart.

Due to the circumstances of the Novel Coronavirus (CoVID-19), our lab had to postpone operations of animal models. Therefore, we could not test the efficacy of the modified substrate. As a result, we began looking further into its conductivity compared to unmodified substrates. We immediately found some extremely promising EIS results for use of PEDOT:PSS modified with CB in low frequency ranges. It is postulated that the PEDOT:PSS is potentially advantageous to PEDOT:PSS/CB in frequency ranges below 10 Hz; however, the aforementioned results indicated high concentrations of CB that have been adequately suspended in PEDOT:PSS result in significant improvements to the impedance at frequency ranges above 10 Hz. This is significantly important for use in our lab, as we have been exploring using LFAC as a potential means to innervate nerve [68–71]. LFAC occurs in frequency ranges between 10 and 50 Hz, well within the limitations of the PEDOT:PSS/CB substrate. Therefore, we believe the PEDOT:PSS/CB will greatly improve our ability to stimulate and record at these frequencies as a result of decreased impedance. Additionally, given the proposed CB-honeycomb structure and its ability to encase the PEDOT:PSS, we believe there are promising results await implantation studies.

Additional modifications may still be explored to improve PEDOT:PSS/CB. It has been recorded that introduction of organic solvents improve the conductivity of the media. The mechanism through which this occurs is still questioned, however it is speculated that some combination of decreasing the Coulombic interactions of the PEDOT and PSS chains, a conformational change, or removal of the PSS insulating shell [33]. Furthermore, dip-treatment of electrodeposited substrate in ethylene glycol may also result in a similar change to what would occur if it the solvent were added prior to deposition, leading to the possibility that simply dip-treating the resulting coated electrode may further improve its conductivity [31, 33, 72].

Carbon black is a relatively cheap substrate compared to other forms of carbon, however it is not very clean nor is it uniform. Potential carbon alternatives that may interact favorably with PEDOT:PSS are carbon nanotubes (cNTs) or graphene. Carbon nanotubes have been explored as a foundation for electrodes, however the addition of PEDOT:PSS via electrodeposition would be novel. An advantageous study would be to compare the interactions of PEDOT:PSS with various carbon structures and additives.

Despite the productive results, there are still some unknowns that arose from our analysis. It appears that the PEDOT:PSS has significantly higher charge capacity than the modified samples, which in theory should increase its conductance. Secondly, it is not clear why the PEDOT:PSS is more effective at lower frequencies, just that the R_0 was significantly smaller for all samples containing the substrate. Due to the use of rapid EIS, the low frequency range is relatively unverifiable. Because the results for rapid EIS in the higher frequencies (10 to 50 kHz) have been clear, it would be advisable to run a series of uncoated electrodes using the original EIS technique, specifying low frequency ranges to be tested and recording their responses to develop a mean response for uncoated electrodes, similar to the frequency sweep performed by Yoshida et al. [73]. The coated electrodes could be then be resubmitted to EIS, using the new testing methodology, which would allow for a complete frequency response for the various CB concentrations tested. The results section (section 2.5.2) for the PEDOT:PSS/CB coating analyzed the low frequency response as if it were correct using the described methods, however it should be stated that although these frequency ranges recorded a response, they are not entirely verifiable. Due to the consistency with the low PEDOT:PSS and PEDOT:PSS/CB concentration impedances at these low frequencies, weak correlations were made. In this extremely low frequency range, it was noted that PEDOT:PSS tended to have low impedance relative to the PEDOT:PSS/CB concentrations, and decreasing PEDOT:PSS/CB concentrations would lead to a response more resembling the pure PEDOT:PSS samples. These correlations were based on the results that electrode size did not significantly vary impedance across the differing electrode lengths, despite equation 2.2 indicating that length will play a role in reducing the relative impedance. Given the results in Fig. 2.11, the assumption was made that there was not a significant impact on uncoated impedance as a result of the size variation. Thus formulating the conclusion that PEDOT:PSS samples posed a more consistent response at frequencies below 10 Hz. That being said, the rapid EIS results indicated the modified compound has significantly improved impedance at mid to high frequencies and approaches R_∞ much more quickly.

Lastly, as the need to develop a more long-term solution for implantable electrodes continues to grow, it may be of interest to look into electrodes made entirely from ICPs. The first steps to doing this could be using a material such as a conductive paint or scaffold that can initiate the deposition of PEDOT:PSS, depositing the substrate and allowing it to grow outward via electrodeposition until a solid electrochemical device has been fabricated from the ICP; analysis of its mechanical and conductive properties could then be performed to test against the solid metal or a metal containing an electroplated ICP. Ultimately, the ideal ICP is a conductive material that can match the mechanical properties of the embedded tissue environment while still maintaining a high degree of conductance across all frequency ranges. For use in our lab, a material that can maintain high conductivity at ranges of 10 – 50 Hz is ideal for our LFAC applications; PEDOT:PSS/CB seems to do the trick.

To satisfy the first aim of this thesis, the recommended PEDOT:PSS/CB concentration and coating method was determined. Results indicated that a PEDOT:PSS/CB samples with a CB concentration of 1 mg/mL should be galvanostatically depositied at a current of 200 μA should be used for 5 minutes. This will ensure an even coating that does not result in agglomeration of the CB on the surface of the electrode, which would potentially lead to an increased probability of the coating being removed through shearing.

4.2 Histology Protocol for Analysis of Nerve Morphology

Prior to the initiation of this project, our lab had no method to analyze nerve tissue on-site. The purpose of Aim 2 was to develop a technique that could be used to study the neural anatomy of various mammals, such as rats, canine, swine, and rabbits. The scope was expanded to include tissue sections from chronic animal models that had electrodes embedded into their peripheral nerves. The PEDOT:PSS/CB electrodes designed in Aim 1 could also be implanted and analyzed. In the scenario of the chronic study, there would be an inflammatory and immune response associated with the implantation of the electrodes that could be very-well understood using the protocol described in Chapter 3. Nevertheless, a sure-fire method for analyzing tissue was developed, as the staining mechanism should stay relatively consistent with what was recorded here.

Histology methods described in the present were applied to the canine vagus nerve of a dog to aid in the deliverables of a DARPA/ LUNA project that measured the nerve diameters to inform development of new neuroprosthetic devices, which led to a measurement of the permittivity of the epineurium-perineurium space. Methods used to perform this staining were described in Section 3.5.2. The results from the NIH funded epineurial impedance paper are anticipating journal review.

LIST OF REFERENCES

[1] P. L. Gildenberg, "History of Electrical Neuromodulation for Chronic Pain: Table 1," *Pain Medicine*, vol. 7, no. suppl 1, pp. S7–S13, May 2006. [Online]. Available: https://academic.oup.com/painmedicine/article-lookup/doi/10.1111/j.1526-4637.2006.00118.x

[2] M. Piccolino, "Animal electricity and the birth of electrophysiology: the legacy of Luigi Galvani," *Brain Research Bulletin*, vol. 46, no. 5, pp. 381–407, Jul. 1998. [Online]. Available: https://linkinghub.elsevier.com/retrieve/pii/S0361923098000264

[3] Fritsch and Hitzig, "Neurologisehe Diagnostik bei endokraniellen Komplikationen yon otorhinologischen Erkrankungen," vol. 183, no. 1, pp. 1–78, Jan. 1964.

[4] R. Bartholow, "Art. I.—Experimental Investigations into the Functions of the Human Brain.:," *The American Journal of the Medical Sciences*, vol. 66, no. 134, pp. 305–313, Apr. 1874. [Online]. Available: http://content.wkhealth.com/linkback/openurl?sid=WKPTLP:landingpage&an=00000441-187404000-00001

[5] J. P. Morgan, "The First Reported Case of Electrical Stimulation of the Human Brain," *Journal of the History of Medicine and Allied Sciences*, vol. XXXVII, no. 1, pp. 51–64, 1982. [Online]. Available: https://academic.oup.com/jhmas/article-lookup/doi/10.1093/jhmas/XXXVII.1.51

[6] J. A. Vilensky and S. Gilman, "Horsley was the first to use electrical stimulation of the human cerebral cortex intraoperatively," *Surgical Neurology*, vol. 58, no. 6, pp. 425–426, Dec. 2002. [Online]. Available: http://www.sciencedirect.com/science/article/pii/S0090301902009205

[7] S. V. Hoesley and R. Clarke, "The Structure and Functions of the Cerebellum Examined by A New Method," pp. 45–124, 1908.

[8] E. A. Spiegel, H. T. Wycis, M. Marks, and A. J. Lee, "Stereotaxic Apparatus for Operations on the Human Brain," *Science*, vol. 106, no. 2754, pp. 349–350, Oct. 1947, publisher: American Association for the Advancement of Science Section: Articles. [Online]. Available: https://science.sciencemag.org/content/106/2754/349

[9] R. Melzack and P. Wall, "Pain Mechanisms: A New Theory," *Science*, vol. 150, no. 3699, pp. 971–979, Nov. 1965. [Online]. Available: https://www.canonsociaalwerk.eu/1846_anesthesie/Canon%20Palliatieve%20Zorg%20-%20Ontstaan%20van%20anesthesie%20-%20Science%20-%20melzackandwallgatecontroltheory.pdf

[10] W. Franks, I. Schenker, P. Schmutz, and A. Hierlemann, "Impedance characterization and modeling of electrodes for biomedical applications," *IEEE Transactions on Biomedical Engineering*, vol. 52, no. 7, pp. 1295–1302, Jul. 2005, conference Name: IEEE Transactions on Biomedical Engineering.

[11] G. Yang, H. Long, H. Tian, S. Luo, and H. Huang, "Bioimpedance Measurement: Modeling of Coplanar Electrodes and Impedance Characterization," in *2008 2nd International Conference on Bioinformatics and Biomedical Engineering*, May 2008, pp. 1248–1251, iSSN: 2151-7622.

[12] M. Sluyters-rehbach, *TERMINOLOGY, NOMENCLATURE AND REPRESENTATION PART I: CELLS WITH METAL ELECTRODES AND LIQUID SOLUTIONS (IUPAC Recommendations 1994)*.

[13] K.-P. Hoffmann, R. Ruff, and W. Poppendieck, "Long-Term Characterization of Electrode Materials for Surface Electrodes in Biopotential Recording," in *2006 International Conference of the IEEE Engineering in Medicine and Biology Society*, Aug. 2006, pp. 2239–2242, iSSN: 1557-170X.

[14] "Double layer capacitance," Apr. 2013. [Online]. Available: https://commons.wikimedia.org/w/index.php?curid=25527676

[15] P. M. Biesheuvel and J. E. Dykstra, "The difference between Faradaic and Nonfaradaic processes in Electrochemistry," *arXiv:1809.02930 [physics]*, Sep. 2018, arXiv: 1809.02930. [Online]. Available: http://arxiv.org/abs/1809.02930

[16] D. Mohilner, "The electrical double layer," *Electrical Analytical Chemistry*, no. 1, pp. 241–409, 1966.

[17] T. Erdey-Grúz, *Kinetics of Electrode Processes*. Wiley, 1972.

[18] A. Bard and L. Faulkner, *Electrochemical Methods*. Wiley, 1980.

[19] E. T. McAdams, A. Lackermeier, J. A. McLaughlin, D. Macken, and J. Jossinet, "The linear and non-linear electrical properties of the electrode-electrolyte interface," *Biosensors and Bioelectronics*, vol. 10, no. 1, pp. 67–74, Jan. 1995. [Online]. Available: http://www.sciencedirect.com/science/article/pii/095656639596795Z

[20] M. R. Abidian and D. C. Martin, "Multifunctional Nanobiomaterials for Neural Interfaces," *Advanced Functional Materials*, vol. 19, no. 4, pp. 573–585, 2009, _eprint: https://onlinelibrary.wiley.com/doi/pdf/10.1002/adfm.200801473. [Online]. Available: https://onlinelibrary.wiley.com/doi/abs/10.1002/adfm.200801473

[21] N. A. Kotov, J. O. Winter, I. P. Clements, E. Jan, B. P. Timko, S. Campidelli, S. Pathak, A. Mazzatenta, C. M. Lieber, M. Prato, R. V. Bellamkonda, G. A. Silva, N. W. S. Kam, F. Patolsky, and L. Ballerini, "Nanomaterials for Neural Interfaces," *Advanced Materials*, vol. 21, no. 40, pp. 3970–4004, 2009, _eprint: https://onlinelibrary.wiley.com/doi/pdf/10.1002/adma.200801984. [Online]. Available: https://onlinelibrary.wiley.com/doi/abs/10.1002/adma.200801984

[22] D. R. Merrill, M. Bikson, and J. G. R. Jefferys, "Electrical stimulation of excitable tissue: design of efficacious and safe protocols," *Journal of Neuroscience Methods*, vol. 141, no. 2, pp. 171–198, Feb. 2005. [Online]. Available: http://www.sciencedirect.com/science/article/pii/S0165027004003826

[23] E. McAdams, J. Jossinet, R. Subramanian, and R. McCauley, "Characterization of gold electrodes in phosphate buffered saline solution by impedance and noise measurements for biological applications," in *2006 International Conference of the IEEE Engineering in Medicine and Biology Society*, Aug. 2006, pp. 4594–4597, iSSN: 1557-170X.

[24] J. Weiland, D. Anderson, and M. Humayun, "In vitro electrical properties for iridium oxide versus titanium nitride stimulating electrodes," *IEEE Transactions on Biomedical Engineering*, vol. 49, no. 12, pp. 1574–1579, Dec. 2002, conference Name: IEEE Transactions on Biomedical Engineering.

[25] J. Riistama and J. Lekkala, "Characteristic properties of implantable Ag/AgCl- and Pt-electrodes," in *The 26th Annual International Conference of the IEEE Engineering in Medicine and Biology Society*, vol. 1, Sep. 2004, pp. 2360–2363.

[26] K. Feron, R. Lim, C. Sherwood, A. Keynes, A. Brichta, and P. C. Dastoor, "Organic Bioelectronics: Materials and Biocompatibility," *International Journal of Molecular Sciences*, vol. 19, no. 8, Aug. 2018. [Online]. Available: https://www.ncbi.nlm.nih.gov/pmc/articles/PMC6121695/

[27] A. Vinckier and G. Semenza, "Measuring elasticity of biological materials by atomic force microscopy," *FEBS Letters*, vol. 430, no. 1, pp. 12–16, Jun. 1998. [Online]. Available: http://www.sciencedirect.com/science/article/pii/S0014579398005924

[28] R. Farraro and R. B. Mclellan, "Temperature dependence of the Young's modulus and shear modulus of pure nickel, platinum, and molybdenum," *Metallurgical Transactions A*, vol. 8, no. 10, pp. 1563–1565, Oct. 1977. [Online]. Available: http://link.springer.com/10.1007/BF02644859

[29] F. S. Bates, G. N. Frederickson, S. L. Aggarwal, J. L. Adams, D. J. Quiram, W. W. Graessley, R. A. Register, D. M. Berggren, D. Nilsson, M. Chen, and D. T. Kugler, "Bi-stable and Dynamic Current Modulation in Electrochemical Organic Transistors," p. 4.

[30] A. MacDiarmid, ""Synthetic Metals": A Novel Role for Organic Polymers (Nobel Lecture)," *Angew. Chem. Int. Ed.*, vol. 40, pp. 2581–2590, 2001.

[31] R. M. Owens and G. G. Malliaras, "Organic Electronics at the Interface with Biology," *MRS Bulletin*, vol. 35, no. 6, pp. 449–456, Jun. 2010. [Online]. Available: https://www.cambridge.org/core/product/identifier/S088376940000083X/type/journal_article

[32] M. Berggren and A. Richter-Dahlfors, "Organic Bioelectronics," *Advanced Materials*, vol. 19, no. 20, pp. 3201–3213, Sep. 2007. [Online]. Available: http://doi.wiley.com/10.1002/adma.200700419

[33] M. O. P. Kara and M. W. Frey, "Effects of solvents on the morphology and conductivity of poly(3,4-ethylenedioxythiophene):Poly(styrenesulfonate) nanofibers," *Journal of Applied Polymer Science*, vol. 131, no. 11, pp. n/a–n/a, Jun. 2014. [Online]. Available: http://doi.wiley.com/10.1002/app.40305

[34] J. Ouyang, ""Secondary doping" methods to significantly enhance the conductivity of PEDOT:PSS for its application as transparent electrode of optoelectronic devices," *Displays*, vol. 34, no. 5, pp. 423–436, Dec. 2013. [Online]. Available: https://linkinghub.elsevier.com/retrieve/pii/S0141938213000668

[35] Y. Xie, S.-H. Zhang, H.-Y. Jiang, H. Zeng, R.-M. Wu, H. Chen, Y.-F. Gao, Y.-Y. Huang, and H.-L. Bai, "Properties of carbon black-PEDOT composite prepared via in-situ chemical oxidative polymerization," *e-Polymers*, vol. 19, no. 1, pp. 61–69, May 2019, publisher: De Gruyter Section: e-Polymers. [Online]. Available: https://www.degruyter.com/view/journals/epoly/19/1/article-p61.xml

[36] K. Kitamura and S. Shiratori, "Layer-by-layer self-assembled mesoporous PEDOT–PSS and carbon black hybrid films for platinum free dye-sensitized-solar-cell counter electrodes," *Nanotechnology*, vol. 22, no. 19, p. 195703, May 2011. [Online]. Available: https://iopscience.iop.org/article/10.1088/0957-4484/22/19/195703

[37] W. M. Grill and J. Thomas Mortimer, "Electrical properties of implant encapsulation tissue," *Annals of Biomedical Engineering*, vol. 22, no. 1, pp. 23–33, Jan. 1994. [Online]. Available: http://link.springer.com/10.1007/BF02368219

[38] A. Lowry, D. Wilcox, E. A. Masson, and P. E. Williams, "Immunohistochemical methods for semiquantitative analysis of collagen content in human peripheral nerve," *Journal of Anatomy*, vol. 191, no. 3, pp. 367–374, Oct. 1997. [Online]. Available: http://doi.wiley.com/10.1046/j.1469-7580.1997.19130367.x

[39] N. Shinowara, M. Michel, and S. Rapoport, "Morphological correlates of permeability in the frog perineurium: Vesicles and ?transcellular channels?" *Cell and Tissue Research*, vol. 227, no. 1, Oct. 1982. [Online]. Available: http://link.springer.com/10.1007/BF00206328

[40] G. Koopmans, B. Hasse, and N. Sinis, "Chapter 19: The role of collagen in peripheral nerve repair," *International Review of Neurobiology*, vol. 87, pp. 363–379, 2009.

[41] S. J. Archibald, C. Krarup, J. Shefner, S.-T. Li, and R. D. Madison, "A collagen-based nerve guide conduit for peripheral nerve repair: An electrophysiological study of nerve regeneration in rodents and nonhuman primates," *The Journal of Comparative Neurology*, vol. 306, no. 4, pp. 685–696, Apr. 1991. [Online]. Available: http://doi.wiley.com/10.1002/cne.903060410

[42] S. F. Cogan, "Neural Stimulation and Recording Electrodes," *Annual Review of Biomedical Engineering*, vol. 10, no. 1, pp. 275–309, 2008, _eprint: https://doi.org/10.1146/annurev.bioeng.10.061807.160518. [Online]. Available: https://doi.org/10.1146/annurev.bioeng.10.061807.160518

[43] J. Hwang, F. Amy, and A. Kahn, "Spectroscopic study on sputtered PEDOT·PSS: Role of surface PSS layer," *Organic Electronics*, vol. 7, no. 5, pp. 387–396, Oct. 2006. [Online]. Available: https://linkinghub.elsevier.com/retrieve/pii/S1566119906000760

[44] Y.-A. Song, A. M. Ibrahim, A. N. Rabie, J. Han, and S. J. Lin, "Microfabricated nerve–electrode interfaces in neural prosthetics and neural engineering," *Biotechnology and Genetic Engineering Reviews*, vol. 29, no. 2, pp. 113–134, Oct. 2013. [Online]. Available: http://www.tandfonline.com/doi/abs/10.1080/02648725.2013.801231

[45] A. L. Hodgkin and A. F. Huxley, "A quantitative description of membrane current and its application to conduction and excitation in nerve," *The Journal of Physiology*, vol. 117, no. 4, pp. 500–544, Aug. 1952. [Online]. Available: https://www.ncbi.nlm.nih.gov/pmc/articles/PMC1392413/

[46] A. Huxley, "From overshoot to voltage clamp," *Trends in Neurosciences*, vol. 25, no. 11, pp. 553–558, Nov. 2002. [Online]. Available: https://linkinghub.elsevier.com/retrieve/pii/S0166223602022804

[47] K. S. Cole, "Dynamic electrical characteristics of the squid axon membrane." no. 3, pp. 253–258, 1949.

[48] E. Daş and A. BayrakçekenYurtcan, "PEDOT/C Composites used as a Proton Exchange Membrane Fuel Cell Catalyst Support: Role of Carbon Amount," *Energy Technology*, vol. 5, no. 9, pp. 1552–1560, 2017, _eprint: https://onlinelibrary.wiley.com/doi/pdf/10.1002/ente.201600779. [Online]. Available: https://onlinelibrary.wiley.com/doi/abs/10.1002/ente.201600779

[49] Y. Xia and J. Ouyang, "PEDOT:PSS films with significantly enhanced conductivities induced by preferential solvation with cosolvents and their application in polymer photovoltaic cells," *Journal of Materials Chemistry*, vol. 21, no. 13, pp. 4927–4936, Mar. 2011, publisher: The Royal Society of Chemistry. [Online]. Available: https://pubs.rsc.org/en/content/articlelanding/2011/jm/c0jm04177g

[50] J. Garcia-Torres and C. Green, "Ternary composite solid-state flexible supercapacitor based on nanocarbons/manganese dioxide/PEDOT:PSS fibres." [Online]. Available: https://upcommons.upc.edu/bitstream/handle/2117/121366/ternary_composite.pdf

[51] U. Lang, E. Müller, N. Naujoks, and J. Dual, "Microscopical Investigations of PEDOT:PSS Thin Films," *Advanced Functional Materials*, vol. 19, no. 8, pp. 1215–1220, 2009, _eprint: https://onlinelibrary.wiley.com/doi/pdf/10.1002/adfm.200801258. [Online]. Available: https://onlinelibrary.wiley.com/doi/abs/10.1002/adfm.200801258

[52] D. R. Sempsrott, "Analysis of the Bioelectric Impedance of the Tissue-Electrode Interface Using a Novel Full-Spectrum Approach," p. 84.

[53] S. Grimnes and O. Martinsen, "Cole electrical impedance Model-a critique and an alternative," *IEEE Transactions on Biomedical Engineering*, vol. 52, no. 1, pp. 132–135, Jan. 2005, conference Name: IEEE Transactions on Biomedical Engineering.

[54] T. Horii, H. Hikawa, M. Katsunuma, and H. Okuzaki, "Synthesis of highly conductive PEDOT:PSS and correlation with hierarchical structure," *Polymer*, vol. 140, pp. 33–38, Mar. 2018. [Online]. Available: https://linkinghub.elsevier.com/retrieve/pii/S0032386118301587

[55] W. M. Grill, S. E. Norman, and R. V. Bellamkonda, "Implanted Neural Interfaces: Biochallenges and Engineered Solutions," *Annual Review of Biomedical Engineering*, vol. 11, no. 1, pp. 1–24, Aug. 2009. [Online]. Available: http://www.annualreviews.org/doi/10.1146/annurev-bioeng-061008-124927

[56] Z. Mornjaković and S. Deschner, "Histology of Peripheral Nerves: Introduction," p. 24.

[57] V. Salonen, M. Lehto, A. Vaheri, H. Aro, and J. Peltonen, "Endoneurial fibrosis following nerve transection: An immunohistological study of collagen types and fibronectin in the rat," *Acta Neuropathologica*, vol. 67, no. 3-4, pp. 315–321, 1985. [Online]. Available: http://link.springer.com/10.1007/BF00687818

[58] R. King, *Atlas of Peripheral Nerve Pathology*, 1st ed., ser. 1. London: Arnold, 1999, vol. 1, no. 1.

[59] G. H. Borschel, K. F. Kia, W. M. Kuzon, and R. G. Dennis, "Mechanical properties of acellular peripheral nerve," *Journal of Surgical Research*, vol. 114, no. 2, pp. 133–139, Oct. 2003, publisher: Elsevier. [Online]. Available: https://www.journalofsurgicalresearch.com/article/S0022-4804(03)00255-5/abstract

[60] S. Jm, K. Ah, and W. Jn, "The characterization of type I and type III collagens from human peripheral nerve." *Biochimica et Biophysica Acta*, vol. 492, no. 2, pp. 415–425, Jun. 1977. [Online]. Available: https://europepmc.org/article/med/328055

[61] S. Peltonen, M. Alanne, and J. Peltonen, "Barriers of the peripheral nerve," *Tissue Barriers*, vol. 1, no. 3, p. e24956, Jul. 2013. [Online]. Available: http://www.tandfonline.com/doi/abs/10.4161/tisb.24956

[62] J.-P. Barral and A. Croibier, "Chapter 1 - Some preliminary thoughts," in *Manual Therapy for the Cranial Nerves*, J.-P. Barral and A. Croibier, Eds. Edinburgh: Churchill Livingstone, Jan. 2009, pp. 1–5. [Online]. Available: http://www.sciencedirect.com/science/article/pii/B9780702031007500045

[63] S. Sunderland, Sir, *Nerve injuries and their repair : a critical appraisal / Sir Sydney Sunderland*. Edinburgh; New York: Churchill Livingstone, 1991. [Online]. Available: https://www.ncbi.nlm.nih.gov/nlmcatalog/9009774

[64] S. K. Lee and S. W. Wolfe, "Peripheral Nerve Injury and Repair," *Journal of the American Academy of Orthopaedic Surgeons*, vol. 8, no. 4, p. 10, 2000.

[65] F. Carson, C. Hladik, and C. Cappellano, "Histotechnology 4e," *Histotechnology*, p. 38, 2015.

[66] P. Seifert, "Toluidine Blue Staining of a 1um, Semi-Thin Epoxy Embedded Tissue Sections," Tech. Rep.

[67] S. Hooten, "Hard Tissue Staining Reference Guide," Mar. 2018.

[68] K. Yoshida and M. R. Horn, "Methods and systems for blocking nerve activity propagation in nerve fibers," US Patent WO2 018 195 332A1, Oct., 2018, library Catalog: Google Patents. [Online]. Available: https://patents.google.com/patent/WO2018195332A1/en

[69] M. R. Horn, C. Ahmed, and K. Yoshida, "Low Frequency Alternating Current Block - A New Method to Stop or Slow Conduction of Action Potentials *," in *2019 9th International IEEE/EMBS Conference on Neural Engineering (NER)*. San Francisco, CA, USA: IEEE, Mar. 2019, pp. 787–790. [Online]. Available: https://ieeexplore.ieee.org/document/8717160/

[70] L. M. Mintch, I. Muzquiz, M. R. Horn, M. Carr, J. H. Schild, and K. Yoshida, "Reversible Conduction Block in Peripheral Mammalian Nerve Using Low Frequency Alternating Current *," in *2019 9th International IEEE/EMBS Conference on Neural Engineering (NER)*. San Francisco, CA, USA: IEEE, Mar. 2019, pp. 823–824. [Online]. Available: https://ieeexplore.ieee.org/document/8716901/

[71] M. I. Muzquiz, "REVERSIBLE NERVE CONDUCTION BLOCK USING LOW FREQUENCY ALTERNATING CURRENTS," p. 103.

[72] T. Horii, H. Hikawa, M. Katsunuma, and H. Okuzaki, "Synthesis of highly conductive PEDOT:PSS and correlation with hierarchical structure," *Polymer*, vol. 140, pp. 33–38, Mar. 2018. [Online]. Available: https://linkinghub.elsevier.com/retrieve/pii/S0032386118301587

[73] K. Yoshida, A. Inmann, and M. Haugland, "Measurment of complex Impedance spectra of implanted electrodes," *ResearchGate*, Jan. 1999. [Online]. Available: https://www.researchgate.net/publication/242748782_MEASUREMENT_OF_COMPLEX_IMPEDANCE_SPECTRA_OF_IMPLANTED_ELECTRODES